Multispectral Hyperbolic Incoherent Holography

MARCH 2019

Department of Electrical Engineering and Computer Science,
Graduate School of Engineering, Iwate University

KEERAYOOT SRINUANJAN

Abstract

This dissertation presents multispectral hyperbolic incoherent holography. The studies include improvement of an experimental method, the mathematical theory used to retrieve the spectral components of three-dimensional (3D) images, a method for in situ calibration of phase aberration, experimental results, and an analytically derived solution of the impulse response function (IRF) of the hyperbolic incoherent holography. The dissertation consists of the following six chapters.

In chapter 1, the author gives an overview of the dissertation. He begins by introducing the research background. Next, the objectives of the research are declared. Subsequently, the structure of the dissertation is presented.

In chapter 2, the author summarizes the theoretical background of the research. He begins by demonstrating the properties of light that can be derived from the wave equation, including the interference phenomena of light waves based on the superposition principle, coherence of light waves and the Fourier transform spectroscopy. The mathematical method used to retrieve the 3D image is demonstrated.

In chapter 3, the author presents a new method to obtain hyperbolic-type volume interferograms. An alternative setting of a two-wavefront folding interferometer is introduced. In this interferometer, the object is fixed but both prisms are moved in steps. A single detector is used instead of an image sensor. In contrast with the conventional method using a two-wavefront folding interferometer, the presented method enables directly measuring the hyperbolic volume interferogram without using the synthetic aperture technique. From the obtained hyperbolic volume interferogram, the spectral profile of an object can be found in a way analogous to Fourier transform spectrometry.

The author demonstrates a mathematical theory that can be used to retrieve spectrally resolved 3D images. The optical intensity of 3D interferograms is first expressed in terms of a spatial correlation function. This function represents the interference of optical fields reflected by the prisms. For a stationary field, the spatial correlation function can be expressed as the Fourier integral of the cross-spectral density where the cross-spectral density is defined as the cross-correlation between the monochromatic components of the optical field. The function is expressed in the form of two-dimensional convolution of the spectral density of the object and the hyperbolic phase factor. Applying those cross-spectral densities, the author demonstrates a

process by which 3D images are retrieved via a modified angular spectrum method. The 3D image of each spectral component can be obtained in this way.

In chapter 4, on the experimental front, the author demonstrates the experimental conditions and results. The measured object is polychromatic. The volume interferogram is measured by the two-wavefront folding interferometer. By applying a Fourier transform to this volume interferogram with respect to the thickness, the spectral profile of the object and the phase distribution of each spectral component of the hyperbolic hologram are obtained. Then 3D images are retrieved form the phase distribution. The experimental results show that the phase distributions do not give the correct 3D images. To address this, the author introduced a method for in situ calibration of phase aberration of the interferometer. In principle, the correct phase distribution for a hyperbolic hologram can be obtained by subtracting the phase aberration from the phase distribution of the measured hyperbolic hologram. The volume interferogram, which records fringe patterns of the phase aberration, and the hyperbolic volume interferogram were measured simultaneously. To perform the experiment, another beam splitter and image sensor were inserted into the interferometer. By applying this calibration method, phase aberration can be eliminated for each cross-spectral density (i.e., for an incoherent hyperbolic hologram). Experimental results showed that the phase aberrations of the two experimental conditions were almost the same. Thus, the phase aberration is reproducible so long as the alignment of the interferometer does not change. By this method, a set of spectral components of three-dimensional images and continuous spectra can be obtained for spatially incoherent, polychromatic objects.

In chapter 5, on the theoretical front, the author investigates the imaging properties of hyperbolic holography by deriving an analytical solution of the IRF. To confirm the mathematical analysis, the images retrieved by analytical solution of the IRF are compared against experimental results.

For mathematical analysis, the author assumes that the object to be measured is a monochromatic point source. The cross-spectral density is then expressed as a Fourier transform of the product of the aperture function and the spatial correlation function. In this, the aperture function represents the extension of the image sensor. To find the IRF and retrieve the image, the angular spectrum method is applied to the cross-spectral density. As a consequence, the final equation appears as a superposed integral of the input image and the IRF, with the IRF expressed in terms of the real and imaginary components of Fresnel integrals.

For comparison, the author applied the angular spectrum method to the cross-spectral density, which consists of an input image function and an IRF. The image is retrieved from the IRF prediction. The author also performs another experiment in which the measured object is a monochromatic point source. The in situ calibration method is applied and an image is retrieved. The two images are compared. The analytical solution of the IRF and the calibration method were confirmed to agree well by this comparison of theoretical and experimental results, suggesting the validity of the method. That is, the images obtained by the proposed method demonstrate the performance of the method.

The final conclusion of the research is stated in chapter 6.

Contents

I Introduction

1.1 Research background

Digital holography uses electronic devices to create a hologram, which can be stored digitally in a computer. In this technique, a light detector or image sensor is used during the recording process and a mathematical method is used during the reconstruction process. When the object is illuminated by incoherent light, the technique is called *digital incoherent holography*. Incoherent holography is based on the self-interference principle, in which light emitted from each point on the object interferes with itself.

In conventional reports of incoherent digital holographic spectrometry, a two-wavefront folding interferometer together with a synthetic aperture technique enables generating a volume interferogram. Several types of volume interferogram have been created by the use of different selection rules in the synthetic aperture technique. These types include the spherical type (S-type) volume interferogram[1–2)], the hyperbolic type (H-type) volume interferogram[3)], and the rotated hyperbolic type (RH-type) volume interferogram[4)] as well as others[5)]. In the S-type method, an analytical solution of a four-dimensional (4D) impulse response function (IRF) is defined and derived over a four-dimensional (x, y, z, ω) space. This solution agrees well with experimental results in terms of spectral resolution and three-dimensional (3D) spatial imaging properties.

This dissertation presents an alternative method, called multispectral hyperbolic incoherent holography. The presented method is based on a new type of two-wavefront folding interferometer. This method has three advanced features. First, it allows directly obtaining the hyperbolic volume interferogram from measurement of the optical intensity on the optical axis of the interferometer. Because a single detector can be used instead of image sensor, interferometric measurement with high sensitivity and high dynamic range is possible. Second, unlike in previous methods, no synthetic aperture technique is required. Third, the object under measurement does not need to be set on an x-y stage. This widens the applicability of the method because spatial translation of the object is not necessary.

1.2 Objectives of the research

The objective of this research was to develop a theoretical basis for multispectral hyperbolic incoherent holography and demonstrate an experimental system of the technique. With this, a hyperbolic volume interferogram can be obtained using a single detector. An alternative design that uses a two-wavefront folding interferometer is also introduced. Phase aberrations occur during measurement with this technique, and a method of calibration to overcome this is proposed. An analytical solution of the IRF of multispectral hyperbolic incoherent holography is derived. The validity of the calibration method was confirmed by experiment and by the obtained analytical solution of the IRF.

1.3 Structure of this dissertation

This dissertation has six chapters. The first chapter is an introduction, giving a research overview and the objectives of the research. Chapter 2 contains a brief survey of background material: the theory of wave properties of light, the principle of superposition, interference of two light waves, coherence of light waves, Fourier transform spectroscopy, reconstruction of spectrally resolved 3D images, and signal processing methods. Chapter 2 is included in part to demonstrate the properties of light that can be represent by mathematical expression in terms of the wave equation. For this purpose, the properties of the interference of light waves are presented, based on the superposition principle and the coherence of light wave. A secondary purpose is to sketch methods of image retrieval based on the angular spectrum method.

Chapter 3 contains a demonstration of the proposed method. How to obtain a 3D volume interferogram from the alternative setting of a two-wavefront folding interferometer is presented. Then, the retrieval process is presented for multispectral components of 3D images. This process is based on the generalized Wiener–Khinchine theorem and a modified version of Van Cittert–Zernike theorem[6]. The experimental conditions, interferometric measurement, and experimental results (without calibration) are shown. From the experimental results, non-ideal properties of the interferometer introduce phase aberration, which degrades the quality of the retrieved image. To resolve this issue, calibration is necessary; an in situ calibration method is presented in chapter 4. In that chapter, the experimental results from image retrieval after calibration to compensate for phase aberration are also shown, and improvement of the image quality is demonstrated.

Chapter 5 includes a theoretical investigation of the 3D imaging properties of hyperbolic holography, making use of a novel analytical solution of the IRF defined over a 4D space.

The primary result obtained in the chapter is a full description of the 4D IRF, which is expressed mathematically in closed form. Theoretical predictions obtained from the analytical solution of IRF are also shown for comparison with experimental results. Finally, all obtained results lead to the conclusion of the dissertation. This is given in chapter 6.

II Foundations of the theory of interference

(Digital incoherent holography)

2.1 Introduction

For coherent holography, the interference pattern of two coherence waves the object wave and the reference wave are captured on a recording medium. The image can then be reconstructed by illuminating hologram with coherent light. For digital incoherent holography, an incoherent wave is used to produce the hologram and an optical sensor is used to record the information. Reconstruction of the image proceeds by using a computer to execute a mathematical method.

In the beginning of this chapter, I will give a brief summary of the mathematical description of light waves. Then I will describe the interference of two light waves that correspond to produce the hologram. After that, an overview of the mathematical method that used to reconstruct the image will be discussed. The chapter then concludes.

2.2 Mathematical description of light waves

Consider Maxwell's equations in the absence of free charge for a propagation medium that is linear, isotropic, homogeneous, and non-dispersive. Under these conditions, the electric field $\boldsymbol{E}$ and magnetic field $\boldsymbol{H}$ obey the wave equations, expressed as

$$\nabla^2 \boldsymbol{E} - \frac{n^2}{c^2}\frac{\partial^2 \boldsymbol{E}}{\partial t^2} = 0 \tag{2.1}$$

$$\nabla^2 \boldsymbol{H} - \frac{n^2}{c^2}\frac{\partial^2 \boldsymbol{H}}{\partial t^2} = 0, \tag{2.2}$$

where $n = \sqrt{\varepsilon/\varepsilon_0}$ is the refractive index of the medium, ε is the electric permittivity in the medium, ε_0 is the electric permittivity in vacuum, $c = 1/\sqrt{\mu_0 \varepsilon_0}$ is the speed of light in vacuum, and μ_0 is the magnetic permeability in vacuum. From these equations, it is possible to summarize the behavior of the electric field $\boldsymbol{E}$ and magnetic field $\boldsymbol{H}$ in three dimensions

as single electromagnetic waves. Further, the propagation of light can be represented by the optical field $V(\boldsymbol{r}, t)$, expressed as

$$\nabla^2 V(\boldsymbol{r},t) - \frac{n^2}{c^2}\frac{\partial^2 V(\boldsymbol{r},t)}{\partial t^2} = 0, \tag{2.3}$$

where $\boldsymbol{r}$ is a (vector) position in space and t is time. Note that in free space, the refractive index n is unity. The symbol $\nabla = \hat{i}\frac{\partial}{\partial x} + \hat{j}\frac{\partial}{\partial y} + \hat{k}\frac{\partial}{\partial z}$ is the vector differential operator, with $\hat{i}$, $\hat{j}$, and $\hat{k}$ the unit vectors in the positive x, y, and z directions, respectively.

For a monochromatic field, the generalized solution of the wave equation can be expressed as the complex function

$$V(\boldsymbol{r}, t) = U(\boldsymbol{r},\omega)\exp(-i\omega t)\,, \tag{2.4}$$

where $U(\boldsymbol{r},\omega)$ is a monochromatic field and $\omega = ck$ is the angular frequency. Substituting Eq. (2.4) into the wave equations yields the Helmholtz equation, expressed as a special case of the wave equation:

$$(\nabla^2 + k^2)U(\boldsymbol{r},\omega) = 0\,. \tag{2.5}$$

In conclusion, electromagnetic waves can represent the propagation of light with an optical field. Therefore, the behavior of light can be described by wave equations.

2.3 Optical wave interference

In this section, I will describe the mathematical representation of the interference between two optical waves. In general, interference between optical waves is understood via the principle of superposition of the two waves. The coherence of the optical field is expressed here mathematically to confirm the interference property of light.

2.3.1 Superposition of two optical waves

When two optical waves of the same frequency combine to form a resultant wave, superposition of the optical waves is used to describe this combination. Consider two waves of optical field with the same amplitude but different phases. These optical fields may be expressed as

$$U_1(\boldsymbol{r}_1, \omega) = a\exp\left[i(\boldsymbol{k}\cdot \boldsymbol{r}_1 + \phi_1(r))\right] \tag{2.6}$$

$$U_2(\boldsymbol{r}_2, \omega) = a\exp\left[i(\boldsymbol{k}\cdot \boldsymbol{r}_2 + \phi_2(r))\right], \tag{2.7}$$

where $\boldsymbol{r}_1$ and $\boldsymbol{r}_2$ are the superposed point measured from the positions of the respective sources and $\phi_1(r)$ and $\phi_2(r)$ are the phases of the respective optical fields. Two optical fields superposed at a fixed point and having different phases may be expressed as

$$\alpha_2 - \alpha_1 = \boldsymbol{k}\cdot(\boldsymbol{r}_2 - \boldsymbol{r}_1) + (\phi_2 - \phi_1). \tag{2.8}$$

Here, $\alpha_1 = \boldsymbol{k}\cdot \boldsymbol{r}_1 + \phi_1$ and $\alpha_2 = \boldsymbol{k}\cdot \boldsymbol{r}_2 + \phi_2$. From the superposition principle, the resultant optical field U_R at the point is

$$\begin{aligned} U_R &= U_1 + U_2 \\ &= a\left[\exp(i\alpha_1) + \exp(i\alpha_2)\right]. \end{aligned} \tag{2.9}$$

2.3.2 Interference of two optical waves

Consider the interference between two optical fields of light waves represented as $V_1(\boldsymbol{r}_1, t)$ and $V_2(\boldsymbol{r}_2, t)$:

$$V_1(\boldsymbol{r}_1, t) = a_1\exp\left[i(\boldsymbol{k}\cdot \boldsymbol{r}_1 - \omega t + \phi_1)\right] \tag{2.10}$$

$$V_2(\boldsymbol{r}_2, t) = a_2\exp\left[i(\boldsymbol{k}\cdot \boldsymbol{r}_2 - \omega t + \phi_2)\right]. \tag{2.11}$$

The principle of superposition means that at some general point P, defined by position vector $\boldsymbol{r}$, the superposed waves will have optical field $V_p(\boldsymbol{r},t)$ given by

$$V_p(\boldsymbol{r},t) = V_1(\boldsymbol{r}_1,t_1) + V_2(\boldsymbol{r}_2,t). \tag{2.12}$$

The intensity at point P is given by

$$\begin{aligned} I(\boldsymbol{r},t) &= \left|V_p(\boldsymbol{r},t)\right|^2 \\ &= \left|V_1(\boldsymbol{r}_1,t)\right|^2 + \left|V_2(\boldsymbol{r}_2,t)\right|^2 + V_1^*(\boldsymbol{r}_1,t)V_2(\boldsymbol{r}_2,t) + V_2^*(\boldsymbol{r}_1,t)V_1(\boldsymbol{r}_2,t) \\ &= I_1 + I_2 + 2\sqrt{I_1 I_2}\cos\delta, \end{aligned} \tag{2.13}$$

where $\delta = (\alpha_2 - \alpha_1)$ is the phase difference between $V_1(\boldsymbol{r}_1, t)$ and $V_2(\boldsymbol{r}_2, t)$. From Eq. (2.13), the first two terms, I_1 and I_2, correspond to the intensities of the individual waves. The last term depends on the phase difference between the waves and is called *the*

interference term. This term is indicated from the wave nature of light.

2.4 Coherence of light waves

This section introduces the physical meaning of coherence. In general, coherence is used to describe the correlation between the phases of a monochromatic light source. Light waves with random phase relationships are called incoherent light, in contrast with light waves with a constant phase relationship (coherent light).

2.4.1 Mathematical representation of multicolor terms

The mathematical representation for an optical field of a single wavelength at time t at a fixed point is expressed as

$$V(t) = a\exp\left[i(-\omega t + \phi)\right]. \tag{2.14}$$

For multicolor or multi-wavelength optical fields with angular frequency ω, the optical field can be obtained by integrating Eq. (2.14) over all occurring wavelengths. The multi-wavelength optical fields can be expressed as a Fourier integral,

$$V(t) = \frac{1}{2\pi}\int_0^\infty A(\omega)\exp\left\{i\left[-\omega t + \phi(\omega)\right]\right\}d\omega, \tag{2.15}$$

where $A(\omega)$ and $\phi(\omega)$ are the amplitude and phase, respectively, of each optical field as functions of the angular frequency ω.

2.4.2 Temporal coherence function and spatial coherence function

There are two types of coherent light wave. The first is temporally coherent, which is related to the spectral purity of the light source; the second type is laterally or spatially coherent, which is related to the size of the source.

2.4.2.1 Temporal coherence function

Temporal coherence is the phase correlation between temporally distinct points of the radiation field of a source along its line of propagation. A light source can be characterized by an average wave train lifetime τ_0, called its coherence time. The coherence time is the

parameter used to characterize temporal coherence; it specifies the duration of time for which a source maintains its phase. The coherence time is related to the coherence length l_t through the relationship

$$l_t = c\tau_0 = \frac{c}{\Delta\upsilon}. \tag{2.16}$$

Then, approximating $\Delta\upsilon$ by the magnitude of its differential from the expression $\upsilon = c/\lambda$, where υ is a frequency, we may also write

$$l_t \cong \frac{\lambda^2}{\Delta\lambda}, \tag{2.17}$$

where $\Delta\lambda$ is the natural line width of the light source.

2.4.2.2 Spatial coherence function

Spatial coherence is the phase correlation between spatially distinct points of a radiation field. The quality of the interference pattern with a wavefront-splitting interferometer depends on the degree of coherence between distinct regions of the wave field at two points of the light sources.

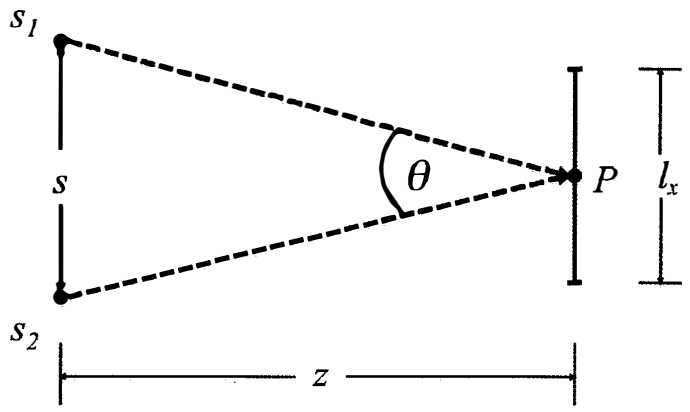

Fig. 2.1 Schematic diagram of coherence width l_x, due to two independent point sources

Consider two point sources, located at S_1 and S_2 as shown in Fig. 2.1. Light propagates and reaches the screen on point P and interference is allowed. The spatial coherence width l_x, is the region of high spatial coherence. This can be express as

$$l_x < \frac{z\lambda}{s} \cong \frac{\lambda}{\theta}, \tag{2.18}$$

where s is the distance between points sources S_1 and S_2, λ is the wavelength of the light sources, and θ is the angle between the line that connect point S_1 to P and the line that connect point S_2 to P (Fig. 2.1).

2.4.3 Mutual coherence function

Consider an interference term of optical fields that originates from two points, where the travel time from their original point to the superposed point are t_1 and t_2, respectively. The spatial correlation function $\Gamma(\boldsymbol{r}_2,\boldsymbol{r}_1,t_2,t_1)$ of this interference is expressed as

$$\Gamma(\boldsymbol{r}_2,\boldsymbol{r}_1,t_2,t_1) = \left\langle V^*(\boldsymbol{r}_2,t_2)V(\boldsymbol{r}_1,t_1)\right\rangle. \tag{2.19}$$

At a fixed point with different paths, the longer path will require additional time $\tau = t_2 - t_1$ to traverse, and the spatial correlation function (or mutual coherence function) of these optical fields is expressed as

$$\Gamma(\boldsymbol{r}_2,\boldsymbol{r}_1,\tau) = \left\langle V^*(\boldsymbol{r}_2,t_2)V(\boldsymbol{r}_1,t_2-\tau)\right\rangle. \tag{2.20}$$

The normalized correlation function (or complex degree of coherence) can be expressed as

$$\gamma(\boldsymbol{r}_2,\boldsymbol{r}_1,\tau) = \frac{\Gamma(\boldsymbol{r}_2,\boldsymbol{r}_1,\tau)}{\sqrt{\Gamma(\boldsymbol{r}_2,\boldsymbol{r}_2,0)}\sqrt{\Gamma(\boldsymbol{r}_1,\boldsymbol{r}_1,0)}}. \tag{2.21}$$

This quantity limits the variation of the interference term and thus controls the contrast in visibility of the fringes as a function of τ.

2.4.4 Fourier transform spectroscopy

The coherence function of a light source can be measured by using a Michelson interferometer. Figure 2.2 shows a schematic diagram of a Michelson interferometer.

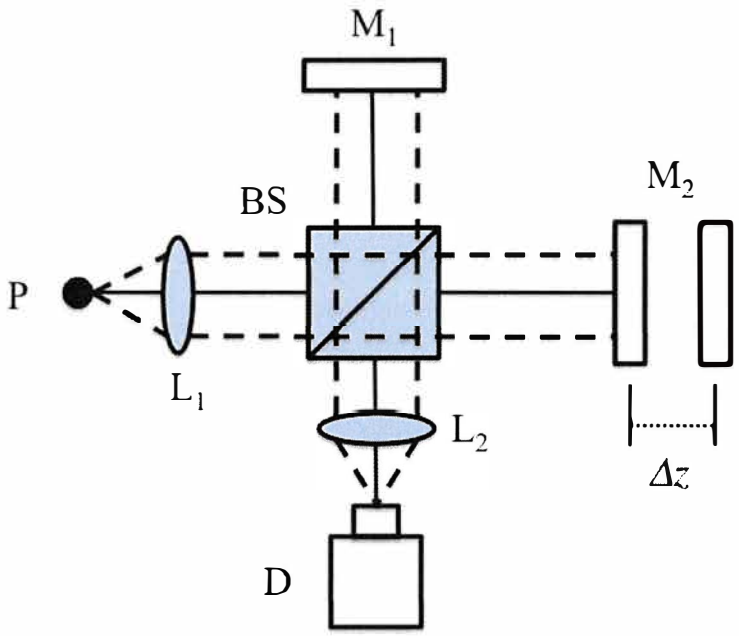

Fig. 2.2 Michelson interferometer

Consider a light source with a continuous spectrum and intensity distribution $S(\omega)$. Suppose the light source is illuminated into a Michelson interferometer. It will propagate from point P to lens L_1, where it is collimated onto the beam splitter (BS). At the BS, the collimated light will be split into two parts (Fig. 2.2). One part is reflected to mirror M_1, and the other part is transmitted to mirror M_2. Both mirrors reflect light back to BS again, superposing the two lights. Each frequency component will produce an interference pattern. Lens L_2 focus the light on a detector (D). The detector records the intensity distribution, which is given by

$$I = c\int_0^\infty S(ck)dk = c\int_0^\infty 2S_0(ck)dk + c\int_0^\infty 2S_0(ck)\cos(kz)dk. \tag{2.22}$$

In this equation, the first term is a constant term, with $S_0(ck)$ as the time-average intensity of each light wave, and the second term is an interference term that depends on the path difference Δz. The intensity fluctuation about the constant bias forms the spectral distribution, given by

$$I(z) = c\int_0^\infty S(ck)\cos(kz)dk. \tag{2.23}$$

The interferogram can be obtained by detecting the output intensity $I(z)$ as a function of the

path difference z at a point on the optical axis of the system. Then, by taking the Fourier transform of the interferogram, the spectral irradiance distribution $S(ck)$ is found as a function of wave number:

$$S(ck) = \frac{2}{\pi c}\int_0^\infty I(z)\cos(kz)dz. \tag{2.24}$$

The minimum resolvable wavelength interval is given by

$$\Delta\lambda = \frac{\lambda^2}{z_W}, \tag{2.25}$$

where z_W is the total path difference, and the resolving power is given by

$$\Re = \frac{\lambda}{\Delta\lambda} = \frac{z_W}{\lambda}. \tag{2.26}$$

2.4.5 Van Cittert–Zernike Theorem

Consider a spatial correlation function $\Gamma(\boldsymbol{r}_1,\boldsymbol{r}_2)$ and a cross-spectral density $W_\omega(P_1,P_2)$, for each wavelength at points P_1 and P_2 on a screen Π. The light source is assumed to be an incoherent source Ω. For simplicity, Ω will be taken to be a portion of a plane parallel to Π. Assume that the linear dimensions of Ω are small relative to the distance OO' between the source and the screen and that the angles between OO' and the lines joining a typical source point a to P_1 and P_2 are small.

Imagine that the source is divided into small elements $d\Omega_1, d\Omega_2, \ldots$ centered on points $a_1, a_2, \ldots$ with linear dimensions that are small compared with the mean wavelength $\overline{\lambda}$. Letting $U_\omega(P_1,t)$ and $U_\omega(P_2,t)$ be the complex disturbances at P_1 and P_2 due to the element $d\Omega_m$, the total disturbances at these points are

$$U_\omega(P_1,t) = \sum_m U_\omega(r_{m1},t), \quad U_\omega(P_2,t) = \sum_m U_\omega(r_{m2},t). \tag{2.27}$$

The cross-spectral density $W_\omega(P_1,P_2)$ for each wavelength at points P_1 and P_2 can be expressed as

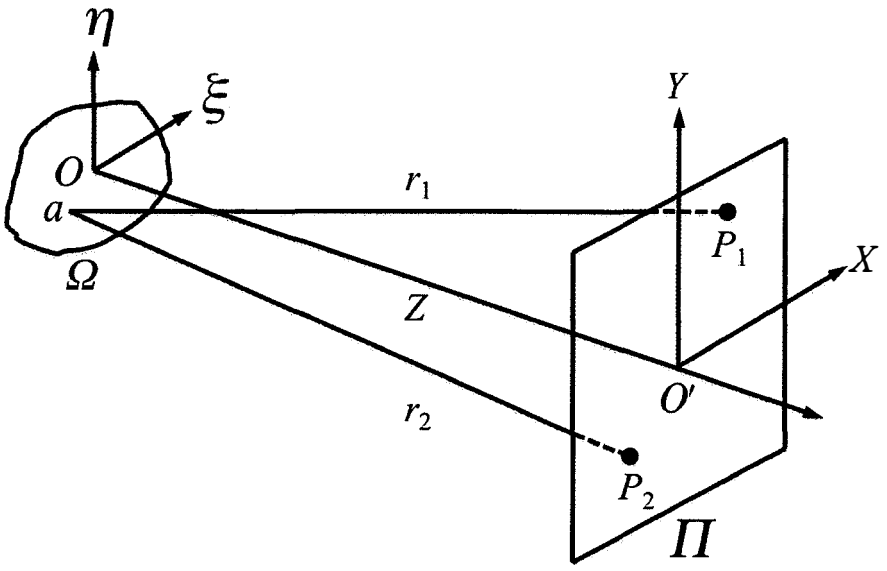

Fig. 2.3 Schematic diagram of the van Cittert–Zernike theorem

$$W_\omega(P_1,P_2) = \left\langle U_\omega^*(P_1,t)U_\omega(P_2,t)\right\rangle$$
$$= \sum_m \left\langle U_\omega^*(\boldsymbol{r}_{m1},t)U_\omega(\boldsymbol{r}_{m2},t)\right\rangle + \sum_{m\neq n}\sum_n \left\langle U_\omega^*(\boldsymbol{r}_{m1},t)U_\omega(\boldsymbol{r}_{n2},t)\right\rangle. \tag{2.28}$$

Assume that the light source is mutually incoherent with zero mean value. Then,

$$\left\langle U_\omega^*(\boldsymbol{r}_{m1},t)U_\omega(\boldsymbol{r}_{n2},t)\right\rangle = 0 \qquad (m\neq n). \tag{2.29}$$

If r_{m1} and r_{m2} are the distances of the source elements $d\Omega_1$ and $d\Omega_2$ to P_1 and P_2, respectively, then

$$U_\omega(\boldsymbol{r}_{m1},t) = \frac{A_m\left(t - r_{m1}/c\right)}{r_{m1}}\exp\left[i(kr_{m1} - \omega t + \phi_m)\right], \tag{2.30}$$

$$U_\omega(\boldsymbol{r}_{m2},t) = \frac{A_m\left(t - r_{m2}/c\right)}{r_{m1}}\exp\left[i(kr_{m2} - \omega t + \phi_m)\right], \tag{2.31}$$

where A_m is the amplitude of the source elements, ϕ_m is the initial phase of the source elements, $k = 2\pi/\lambda$ is the wave number, and $r_{m1} = |\boldsymbol{r}_{m1}|$ and $r_{m2} = |\boldsymbol{r}_{m2}|$ are the magnitudes of the position vectors $\boldsymbol{r}_{m1}$ and $\boldsymbol{r}_{m2}$, respectively.

Hence,

$$\left\langle U_\omega^*(P_1,t)U_\omega(P_2,t)\right\rangle = \left\langle A_m^*\left(t - r_{m1}/c\right)A_m\left(t - r_{m2}/c\right)\right\rangle \frac{\exp[ik(r_{m2}-r_{m1})]}{r_{m1}r_{m2}}$$

$$= \left\langle A_m^*(t)A_m\left(t - \frac{r_{m2}-r_{m1}}{c}\right)\right\rangle \frac{\exp[ik(r_{m2}-r_{m1})]}{r_{m1}r_{m2}}. \tag{2.32}$$

When the path difference $r_{m2} - r_{m1}$ is small compared with the coherence length of the light, the retardation $(r_{m2} - r_{m1})/c$ in the argument of A_m^* may be neglected, giving us, from Eqs. (2.28), (2.30), and (2.31), the following.

$$W_{\bar{\omega}}(P_1,P_2) = \sum_m \left\langle A_m^*(t)A_m(t)\right\rangle \frac{\exp[ik(r_{m2}-r_{m1})]}{r_{m1}r_{m2}} \tag{2.33}$$

The quantity $\left\langle A_m^*(t)A_m(t)\right\rangle$ characterizes the intensity of the radiation from the source to the element $d\Omega_m$. For a large number of the source elements, the source may be regarded as effectively continuous. Let $S(a)$ be the intensity per unit area of the source; that is, let $S(a_m)d\Omega_m = \left\langle A_m^*(t)A_m(t)\right\rangle$. Then, Eq. (2.33) becomes

$$W_\omega(\boldsymbol{r}_1,\boldsymbol{r}_2) = \int_\Omega S(a)\frac{\exp[ik(r_{m2}-r_{m1})]}{r_{m1}r_{m2}}da. \tag{2.34}$$

If the intensity $S(a)$ is uniform, then the corresponding diffraction is the diffraction of a spherical wave of uniform amplitude by an aperture of the same size and shape as the source. If we let (ξ,η) be the coordinates of a typical source point a with origin O and let (X_1,Y_1) and (X_2,Y_2) be the coordinates of points P_1 and P_2 along parallel axes with origin O', then Z denotes the distance OO'. Assuming the paraxial approximation and using binomial expansion, the distance between r_1 and r_2 can be written

$$r_2 - r_1 = \frac{(X_2^2+Y_2^2)-(X_1^2+Y_1^2)}{2Z} - \frac{(X_2-X_1)\xi+(Y_2-Y_1)\eta}{Z}. \tag{2.35}$$

Let us define new parameters:

$$\alpha = \frac{(X_2-X_1)}{Z},\quad \beta = \frac{(Y_2-Y_1)}{Z},\quad \varphi = \frac{k\left[(X_2^2+Y_2^2)-(X_1^2+Y_1^2)\right]}{2Z}, \tag{2.36}$$

The complex degree of coherence or spectral degree of coherence $\mu_\omega(\boldsymbol{r}_1,\boldsymbol{r}_2)$ is then given by

$$\mu_\omega(\boldsymbol{r}_1,\boldsymbol{r}_2) = \frac{W_\omega(\boldsymbol{r}_1,\boldsymbol{r}_2)}{\sqrt{W_\omega(\boldsymbol{r}_1,\boldsymbol{r}_1)}\sqrt{W_\omega(\boldsymbol{r}_2,\boldsymbol{r}_2)}}$$

$$= \frac{\exp(i\varphi)\int_{\Omega} S_{\omega}(\xi,\eta)\exp\left[-ik(\alpha\xi+\beta\eta)\right]d\xi d\eta}{\int_{\Omega} S_{\omega}(\xi,\eta)d\xi d\eta}. \tag{2.37}$$

Hence, if the linear dimensions of the source and the distance between points P_1 and P_2 are small relative to the distance of these points from the source, the degree of coherence $|\mu_{\omega}(\boldsymbol{r}_1,\boldsymbol{r}_2)|$ is equal to the absolute value of the normalized Fourier transform of the spectral density function of the source.

For a uniform circular source of diameter ρ with its center at O, integrating Eq. (2.37) gives

$$\mu_{\omega}(\boldsymbol{r}_1,\boldsymbol{r}_2) = \left(\frac{2J_1(\upsilon)}{\upsilon}\right)\exp(i\varphi), \tag{2.38}$$

where $\upsilon = \bar{k}\rho\sqrt{\alpha^2 + \beta^2/2}$ and $J_1(\upsilon)$ are, respectively, the Bessel functions of the first kind and first order. The value $|2J_1(\upsilon)/\upsilon|$ decreases steadily from unity when $\upsilon = 0$, reaching zero when $\upsilon = 3.83$; thus, as the point P_1 and P_2 become increasingly separated, the degree of coherence steadily decreases. Complete incoherence occurs when P_1 and P_2 are separated by the distance

$$P_1P_2 = \frac{1.22Z\lambda}{\rho}. \tag{2.39}$$

This result is useful in estimating the size of source needed in experiments on interference and diffraction.

2.5 3D image reproduction from cross-spectral density (Angular spectrum method)

In general, interferometric measurement is based on observation of the mutual coherence function $\Gamma(\boldsymbol{r}',t';\boldsymbol{r},t)$, which represents the correlation between field amplitudes at a pair of space–time points. For stationary fields, the mutual coherence function is expressed as a Fourier transform of the cross-spectral density $W_{\omega}(\boldsymbol{r}',\boldsymbol{r})$, where the frequency is ω.

$$\Gamma(\boldsymbol{r}',\boldsymbol{r},\tau) = \int_0^{+\infty} \exp(-i\omega\tau) W_\omega(\boldsymbol{r}',\boldsymbol{r}) d\omega \tag{2.40}$$

Here, $\tau = t - t'$ is the time difference. Consider a physical situation in which a polychromatic optical field propagates in the positive z direction and occupies all of the space. This space is assumed to be homogeneous and source free. To begin, we consider a monochromatic field. The optical field is represented by the complex scalar function $U_\omega(\boldsymbol{r})$. Throughout the space, the optical field satisfies the Helmholtz equation:

$$(\nabla^2 + k^2) U_\omega(\boldsymbol{r}) = 0, \tag{2.41}$$

where $k = \omega/c$, and c is the speed of light in vacuum. Let us define the position vectors $\boldsymbol{r}_\perp = (x,y)$, where $\boldsymbol{r} = (x,y,z) = (\boldsymbol{r}_\perp, z)$, and $\boldsymbol{r}_\perp' = (x',y')$, where $\boldsymbol{r}' = (x',y',z) = (\boldsymbol{r}_\perp', z)$. The state of coherence of the optical field in a given plane $z =$ constant is specified by the cross-spectral density,

$$W_\omega^{(z)}(\boldsymbol{r}_\perp', \boldsymbol{r}_\perp) = \left\langle U_\omega^*(\boldsymbol{r}_\perp', z) U_\omega(\boldsymbol{r}_\perp, z) \right\rangle, \tag{2.42}$$

where the angle bracket $\langle \ldots \rangle$ indicates an ensemble average and the position of the reference plane is noted in superscript parentheses.

To treat the propagation of the optical field and the cross-spectral density, we express the optical field $U_\omega(\boldsymbol{r}) = U_\omega(\boldsymbol{r}_\perp, z)$ as a two-dimensional Fourier integral with respect to $\boldsymbol{r}_\perp$:

$$U_\omega(\boldsymbol{r}_\perp, z) = \frac{1}{2\pi} \int \tilde{U}_\omega(\boldsymbol{k}_\perp, z) \exp(i\boldsymbol{k}_\perp \cdot \boldsymbol{r}_\perp) d^2 k_\perp, \tag{2.43}$$

where $\tilde{U}_\omega(\boldsymbol{k}_\perp, z)$ is the Fourier amplitude and $\boldsymbol{k} = (k_x, k_y, k_z) = (\boldsymbol{k}_\perp, k_z)$ is the wave-number vector. The optical field in the Fourier domain $\tilde{U}_\omega(\boldsymbol{k}_\perp, z)$ is related to the optical field in the spatial domain $U_\omega(\boldsymbol{r}_\perp, z)$ via the inverse Fourier transform, expressed as

$$\tilde{U}_\omega(\boldsymbol{k}_\perp, z) = \frac{1}{2\pi} \int U_\omega(\boldsymbol{r}_\perp, z) \exp(-i\boldsymbol{k}_\perp \cdot \boldsymbol{r}_\perp) d^2 r_\perp. \tag{2.44}$$

Substitution of Eq. (2.43) into Eq. (2.41) leads to the equation that describes the z evolution of the Fourier amplitude $\tilde{U}_\omega(\boldsymbol{k}_\perp, z)$:

$$\left(\frac{\partial^2}{\partial z^2} + k_z^2 \right) \tilde{U}_\omega(\boldsymbol{k}_\perp, z) = 0, \tag{2.45}$$

where

$$k_z = \begin{cases} [k^2 - \boldsymbol{k}_\perp^2]^{1/2} & \text{if} \quad k_\perp \le k \\ i[\boldsymbol{k}_\perp^2 - k^2]^{1/2} & \text{if} \quad k_\perp \ge k \end{cases} \tag{2.46}$$

is the z component of the wave-number vector as a function of $\boldsymbol{k}_\perp$. Then, the Fourier amplitude, traveling in the direction of increasing z, obeys the propagation law

$$\tilde{U}_\omega(\boldsymbol{k}_\perp, z) = \exp[ik_z(z - z')]\tilde{U}_\omega(\boldsymbol{k}_\perp, z'). \tag{2.47}$$

Equation (2.46) implies that where $k_\perp \le k$, the waves are traveling waves and where $k_\perp \ge k$, the waves are evanescent waves. For our purposes, we will ignore the evanescent waves. From the previous equation, Eq. (2.44), the four-dimensional Fourier transform of the cross-spectral density is expressed as

$$\begin{aligned} \tilde{W}_\omega^{(z)}(\boldsymbol{k}_\perp', \boldsymbol{k}_\perp) &= \left\langle \tilde{U}_\omega^*(\boldsymbol{k}_\perp', z)\tilde{U}_\omega(\boldsymbol{k}_\perp, z) \right\rangle \\ &= \frac{1}{(2\pi)^2} \int \left\langle U_\omega^*(\boldsymbol{r}_\perp', z)U_\omega(\boldsymbol{r}_\perp, z) \right\rangle \exp[-i(\boldsymbol{k}_\perp \cdot \boldsymbol{r}_\perp - \boldsymbol{k}_\perp' \cdot \boldsymbol{r}_\perp')] d^2\boldsymbol{r}_\perp' d^2\boldsymbol{r}_\perp \\ &= \frac{1}{(2\pi)^2} \int W_\omega^{(z)}(\boldsymbol{r}_\perp', \boldsymbol{r}_\perp) \exp[-i(\boldsymbol{k}_\perp \cdot \boldsymbol{r}_\perp - \boldsymbol{k}_\perp' \cdot \boldsymbol{r}_\perp')] d^2\boldsymbol{r}_\perp' d^2\boldsymbol{r}_\perp, \end{aligned} \tag{2.48}$$

where we use Eq. (2.42) and substitute Eq. (2.47) into the final expression of Eq. (2.48). The propagation law of $\tilde{W}_\omega^{(z)}(\boldsymbol{k}_\perp', \boldsymbol{k}_\perp)$ is written as

$$\tilde{W}_\omega^{(z)}(\boldsymbol{k}_\perp', \boldsymbol{k}_\perp) = \exp[i(k_z - k_z')(z - z')]\tilde{W}_\omega^{(z')}(\boldsymbol{k}_\perp', \boldsymbol{k}_\perp), \tag{2.49}$$

where k_z' is given by a primed version of Eq. (2.46). The back propagation law, which is represented by the relationship between the cross-spectral densities in the Fourier domain at distances z_0 and $z_0 - z'$, may be expressed as

$$\tilde{W}_\omega^{(z_0 - z')}(\boldsymbol{k}_\perp', \boldsymbol{k}_\perp) = \exp[-i(k_z - k_z')z']\tilde{W}_\omega^{(z_0)}(\boldsymbol{k}_\perp', \boldsymbol{k}_\perp). \tag{2.50}$$

In this, the exponential term $\exp[-i(k_z - k_z')z']$ denotes the optical transfer function (OTF). The four-dimensional Fourier transform of the cross-spectral density at distance $z = z_0 - z'$ may be written as

$$\tilde{W}_\omega^{(z_0 - z')}(\boldsymbol{k}_\perp', \boldsymbol{k}_\perp) = \frac{1}{(2\pi)^2} \int W_\omega^{(z_0 - z')}(\boldsymbol{r}_\perp', \boldsymbol{r}_\perp) \exp[-i(\boldsymbol{k}_\perp \cdot \boldsymbol{r}_\perp - \boldsymbol{k}_\perp' \cdot \boldsymbol{r}_\perp')] d^2\boldsymbol{r}_\perp' d^2\boldsymbol{r}_\perp. \tag{2.51}$$

According to Eqs. (2.48), (2.50), and (2.51), we may obtain the relationship between the cross-spectral densities at distances $z = z_0$ and $z = z_0 - z'$ by the diagram shown in Fig. 2.4.

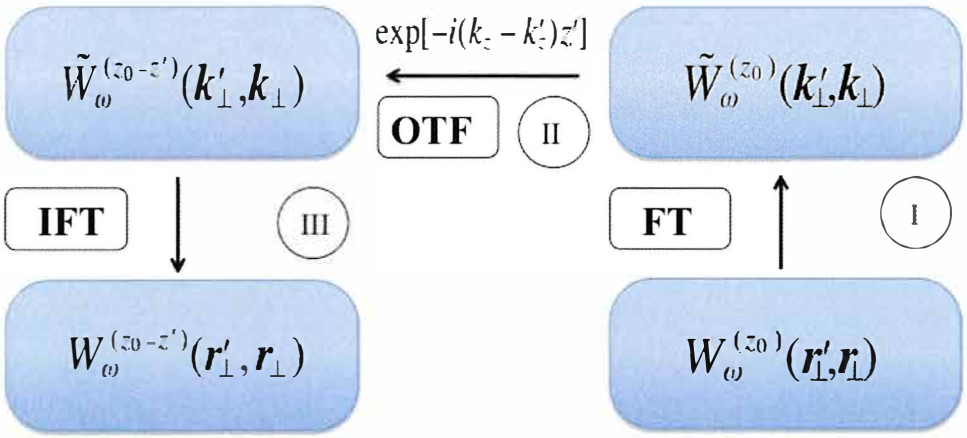

Fig. 2.4 Diagram of angular spectrum method

From Fig. 2.4, the process starts by taking the Fourier transform of the cross-spectral density at the input distance. The cross-spectral density in the Fourier domain is then obtained. After that, it is multiplied by the OTF. It becomes the cross-spectral density in the Fourier domain at the output distance. Then, the inverse Fourier transform is applied. Finally, the cross-spectral density at the output distance is obtained.

2.6 Conclusion

From Maxwell's equations, the behavior of light can be explained by a mathematical expression, and specifically by a wave equation. One property of light waves is interference based on the superposition principle. The mathematical representation of interference between two optical waves has three terms to consider. The first two terms are constant terms that depend on the intensities of the individual optical waves. The last term, the *interference term*, is a fluctuation term that depends on the interference between the two optical waves. This term confirms the wave nature of light. The interference term depends on the coherence of the light waves. There are two types of coherence functions: temporal and spatial. Coherence can be identified by degree of coherence or by a normalized correlation function. A Michelson interferometer allows measurement of the temporal coherence length. Moreover, by taking a Fourier transform of an interferogram, the spectral distribution of the light source can be

found. From the Van Cittert–Zernike theorem, the spatial coherence function can also be found.

The method for reproduction of an image (i.e., the angular spectrum method) is demonstrated here. In the angular spectrum method, the relationship between the cross-spectral density at the input field and the cross-spectral density at the output field are connected via the angular cross-spectral density. Taking a Fourier transform, multiplying by the OTF, and taking the inverse Fourier transform, one can obtain the cross-spectral density at the output distance. From the foundations and theory of interference, the principles can be applied to the recording and retrieval processes of incoherent holography. This will be demonstrated in the next chapter.

III Two-wavefront folding interferometer

3.1 Introduction

In this chapter, I summarize a method of creating a 3D volume interferogram by making use of a two-wavefront folding interferometer with alternative settings. Unlike in conventional methods, the two-wavefront folding interferometer was adjusted in steps and a single detector was used instead of an image sensor. This allows direct measurement of the hyperbolic volume interferogram.

In the conventional setting with an interferometer, the object under measurement is moved. Because of this, a synthetic aperture technique is required. In the method described here, the position of the object is fixed but both prisms are moved stepwise. The optical intensity on the optical axis and are recorded after each movement of the prisms and a piezoelectric translator (PZT). All optical intensities are arranged three-dimensionally to obtain the hyperbolic volume interferogram. This method does not require using a synthetic aperture technique.

I also show the mathematical description used to retrieve a 3D image. The method is a twice-repeated Fourier transform method (angular spectrum method in chapter 2) in which light propagation is treated as a unit of a plane wave based on propagation of the angular spectrum. In the process the cross-spectral density across a reference plane is first written in terms of the angular cross-spectral density in Fourier space. The relationship between the angular cross-spectral density across the reference plane and a given source plane is then obtained via an optical transfer function (OTF). Finally, the cross-spectral density across the source plane is retrieved.

3.2 Measurement of 3D volume interferogram

In this work, a two-wavefront folding interferometer was used to measure a volume interferogram. Figure 3.1 shows a schematic diagram of the experimental system. The measured 3D object is spatially incoherent and polychromatic. The propagated light is split by a beam splitter (BS). Each split wavefront is reversed from up to down by prism P or from left

to right by prism P' and then superposed on the BS again. After passing through the lens, only the optical intensity on the optical axis at the apex of prism P' is detected by a single detector. In this interferometer, the lateral shears, denoted (X,Y), are introduced by the x and y stages. Initially, the optical path lengths, measured from the apex of prisms P and P' to the origin of the Cartesian coordinate system, are set at equal distance. A longitudinal shear, denoted Z, is introduced by the PZT. The optical path length between one of apex of prism P' and the origin of the Cartesian coordinate system (x,y) is denoted by z_0. During interferometric measurement, the x and y stages and the PZT are moved stepwise, and the optical intensities at the same position on the optical axis are recorded after each movement. After all measurements, the optical intensities at every position are arranged sequentially in 3D space (X,Y,Z), according to the motions of the stages. In this way, the hyperbolic volume interferogram can be obtained directly.

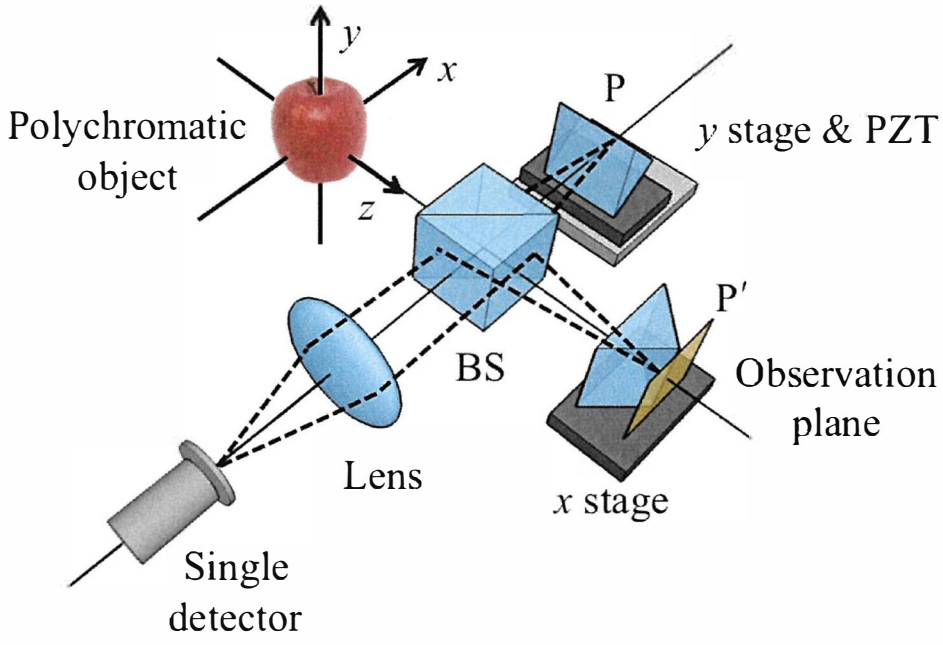

Fig. 3.1 Schematic diagram of experimental system

The superposed points of the optical fields reflected by the prisms P and P' are expressed as $\boldsymbol{r}=(x,Y-y,z_0+Z)$ and $\boldsymbol{r}'=(X-x,y,z_0)$, respectively. The optical intensity of the 3D interferogram, $I(X,Y,Z)$, is expressed in the following form:

$$I(X,Y,Z)=\frac{1}{4}\left[\Gamma(\boldsymbol{r},\boldsymbol{r})+\Gamma(\boldsymbol{r}',\boldsymbol{r}')+\Gamma(\boldsymbol{r}',\boldsymbol{r})+\Gamma^{*}(\boldsymbol{r}',\boldsymbol{r})\right], \tag{3.1}$$

where * denotes complex conjugation. In this equation, the time t in Γ is suppressed because the optical field is stationary in time. In Eq. (3.1), $\Gamma(\boldsymbol{r},\boldsymbol{r}) = \langle |V(\boldsymbol{r},t)|^2 \rangle$ and $\Gamma(\boldsymbol{r}',\boldsymbol{r}') = \langle |V(\boldsymbol{r}',t)|^2 \rangle$ are the optical intensities of the optical field $V(\boldsymbol{r},t)$ at points $\boldsymbol{r}$ and $\boldsymbol{r}'$ respectively, and $\langle \ldots \rangle$ stands for the ensemble average. In this method, only those intensities on the optical axis are detected. The 3D position vectors are then rewritten by setting $x = y = 0$, as $\boldsymbol{r} = (0, Y, z_0 + Z)$ and $\boldsymbol{r}' = (X, 0, z_0)$.

For a stationary field, the spatial correlation function $\Gamma(X,0,z_0;0,Y,z_0+Z)$ recorded in the 3D volume interferogram may be expressed as a superposition of the cross-spectral density $W_\omega(X,0,z_0;0,Y,z_0+Z)$ in the form

$$\Gamma(X,0,z_0;0,Y,z_0+Z) = \int_0^\infty W_\omega(X,0,z_0;0,Y,z_0+Z)d\omega, \tag{3.2}$$

where $\omega = ck$ is the angular frequency, c is the speed of light in free space, and $k = 2\pi/\lambda$ is the wavenumber with wavelength λ. Equation (3.2) means that, for a stationary optical field, the spectral components of the optical fields of different frequencies are mutually uncorrelated. Under the paraxial approximation and the assumptions $z_0 >> Z$ and $z_0 >> z_s$, the cross-spectral density W_ω appearing in the right-hand-side of Eq. (3.2) can be written in the following form:

$$W_\omega(X,0,z_0;0,Y,z_0+Z) = \exp(ikZ)W_\omega(X,0,z_0;0,Y,z_0). \tag{3.3}$$

On substituting Eq. (3.3) into Eq. (3.2), the relation between the measured spatial correlation function Γ and the cross-spectral density W_ω can be obtained as

$$\Gamma(X,0,z_0;0,Y,z_0+Z) = c\int_0^\infty \exp(ikZ)W_\omega(X,0,z_0;0,Y,z_0)dk. \tag{3.4}$$

It is then clear that Eq. (3.4) may be inverted to express the cross-spectral density W_ω as the Fourier transform of the spatial correlation function Γ:

$$W_\omega(X,0,z_0;0,Y,z_0) = \frac{1}{2\pi c}\int \Gamma(X,0,z_0;0,Y,z_0+Z)\exp(-ikZ)dZ. \tag{3.5}$$

The integration is over the actual extension of the interferogram with respect to the thickness Z. The cross-spectral density $W_\omega(X,0,z_0;0,Y,z_0)$ is defined as the cross-correlation between the monochromatic component of the optical fields $U_\omega(X,0,z_0)$ and $U_\omega(0,Y,z_0)$. It is expressed in the following form (for details, see Eq. (A.7) in the Appendix):

$$W_\omega(X,0,z_0;0,Y,z_0) = \langle U_\omega^*(X,0,z_0)U_\omega(0,Y,z_0)\rangle,$$

$$= S'(x_s,y_s,z_s)\otimes\exp\left[i\frac{k}{2z}(-X^2+Y^2)\right], \tag{3.6}$$

where $S'(x_s,y_s,z_s)$ denotes the product of the spectral density of the object at point (x_s,y_s,z_s) and the point-dependent phase factor, the operator $\otimes$ indicates two-dimensional convolution, and $z = z_0 - z_s$ is the optical depth distance of the light source. Figure 3.2 shows a typical hyperbolic volume interferogram as obtained by the method described here. This interferogram corresponds to a monochromatic point source located at the upper left ($x_s < 0$ and $y_s > 0$) of the Cartesian coordinate system. As shown in Eq. (3.6), the sign of the quadratic phase factors of X and Y are opposite. Therefore, the fringe patterns within the volume interferogram are arranged as a hyperbolic surface, as shown in Fig. 3.2.

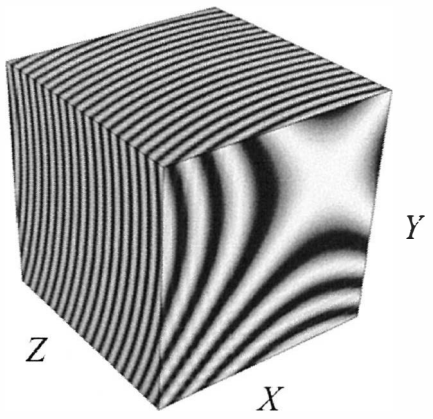

Fig. 3.2 Example of a typical hyperbolic volume interferogram for a monochromatic point source located at the upper left of the Cartesian coordinate system.

3.3 Retrieval of 3D images for many spectral components

The spectral components of 3D images of the object may be retrieved from the hyperbolic volume interferogram by applying a method similar to the inverse propagation of an optical field by the Fresnel diffraction formula. Broadly, there are two methods to retrieve images from hyperbolic holograms: the one-time Fourier transform method (1-FT method) and

two-times Fourier transform method (2-FT method). The 1-FT method treats light propagation as a unit of a spherical wave based on the Huygens–Fresnel principle. The 2-FT method treats light propagation as a unit of a plane wave based on propagation of the angular spectrum. A useful feature of the 2-FT method is that the field of view does not depend on the depth distance. Therefore, this method provides the correct intensity distribution along the z axis and the size of retrieved image does not change. In contrast, the 1-FT method keeps the same field of view but the size of the retrieved image changes. The retrieval process discussed here is based on the 2-FT method. To begin, let us write the cross-spectral density W_ω across a reference plane $z = z_0$ as

$$W_\omega^{(z_0)}(X,0;0,Y) = W_\omega(X,0,z_0;0,Y,z_0)$$
$$= \langle U_\omega^*(X,0,z_0)U_\omega(0,Y,z_0)\rangle, \tag{3.7}$$

where the superscript in the left-hand-side of Eq. (3.7) specifies the position of the reference plane. By taking 2D Fourier transforms of the cross-spectral density in Eq. (3.7), the angular cross-spectral density in Fourier space, denoted $\tilde{W}_\omega^{(z_0)}$, is defined by

$$\tilde{W}_\omega^{(z_0)}(k_x,0;0,k_y) = \frac{1}{2\pi}\int W_\omega^{(z_0)}(X,0;0,Y)\exp[-i(-k_xX + k_yY)]dXdY$$
$$= \langle \tilde{U}_\omega^*(k_x,0,z_0)\tilde{U}_\omega(0,k_y,z_0)\rangle. \tag{3.8}$$

From Eq. (3.8), the angular cross-spectral density defined in the Fourier space $\tilde{W}_\omega^{(z_0-z')}$ across a certain source plane $z = z' < z_0$ can be retrieved. By multiplying this with the inverse of OTF, the relation between the angular cross-spectral densities at $z = z_0 - z'$ and $z = z_0$ can be obtained as

$$\tilde{W}_\omega^{(z_0-z')}(k_x,0;0,k_y) = \frac{\lambda z}{2\pi}\exp\left[i\frac{z'}{2k}(-k_x{}^2 + k_y{}^2)\right]\tilde{W}_\omega^{(z_0)}(k_x,0;0,k_y), \tag{3.9}$$

where k_x and k_y are the lateral components of the wavenumber vector $\boldsymbol{k}$. By taking the inverse Fourier transform of both sides of Eq. (3.9), the cross-spectral density across the source plane $W_\omega^{(z_0-z')}$ is obtained as Eq. (3.10). See Eq. (A.14) of the Appendix for details.

$$W_\omega^{(z_0-z')}(X,0;0,Y) = W_\omega^{(z_0)}(X,0;0,Y)\otimes\exp\left[-i\frac{k}{2z'}(-X^2+Y^2)\right] \tag{3.10}$$

As is seen in Eqs. (3.6), (3.7), and (3.10), this cross-spectral density $W_\omega^{(z_0-z')}$ is proportional to the spectral density $S'(x_s,y_s,z_s)$ at an object plane $z = z_s$. It is then possible to retrieve

the spectral component of a 3D image of the light source by applying a method similar to the conventional angular spectrum technique. In this manner, the 3D spatial distribution of the spectral density (i.e., the 3D image at each spectral component) can be obtained.

3.4 Conclusion

The relation between the volume interferogram and the spatial correlation function can be obtained by the measurement method given here. Then, the cross-spectral density of each spectrum can be expressed in terms of a Fourier transform of the spatial correlation function. The spectral profile of the object is also obtained. For a monochromatic point source, solving analytically shows that the cross-spectral density is in the form of a two-dimensional convolution of the spectral density of the object and the impulse respond function. As a consequence, the fringe patterns within the volume interferogram are arranged as a hyperbolic surface, which is called a hyperbolic volume interferogram.

Using the hyperbolic volume interferogram, the angular spectrum method (2-FT method) was used to retrieve the hyperbolic hologram. This method gives the 3D image at each spectral component. Some experiments and their results will be described in the next chapter to demonstrate this.

IV Experiment and in situ calibration method

4.1 Introduction

This chapter presents the experimental conditions and results. The object being measured is polychromatic. A two-wavefront folding interferometer is used to measure the volume interferogram, obtaining a hyperbolic volume interferogram. The spectral profile of the object and the phase distribution of each spectral component of the hyperbolic hologram can be obtained by applying a Fourier transform to this volume interferogram with respect to the thickness *Z*. However, the phase distributions do not give the correct 3D image. To address this, an in situ calibration method is demonstrated. The phase distribution after calibration is used in the retrieval process, and then the shape and size of the retrieved image are compared against the true values.

4.2 Experimental conditions

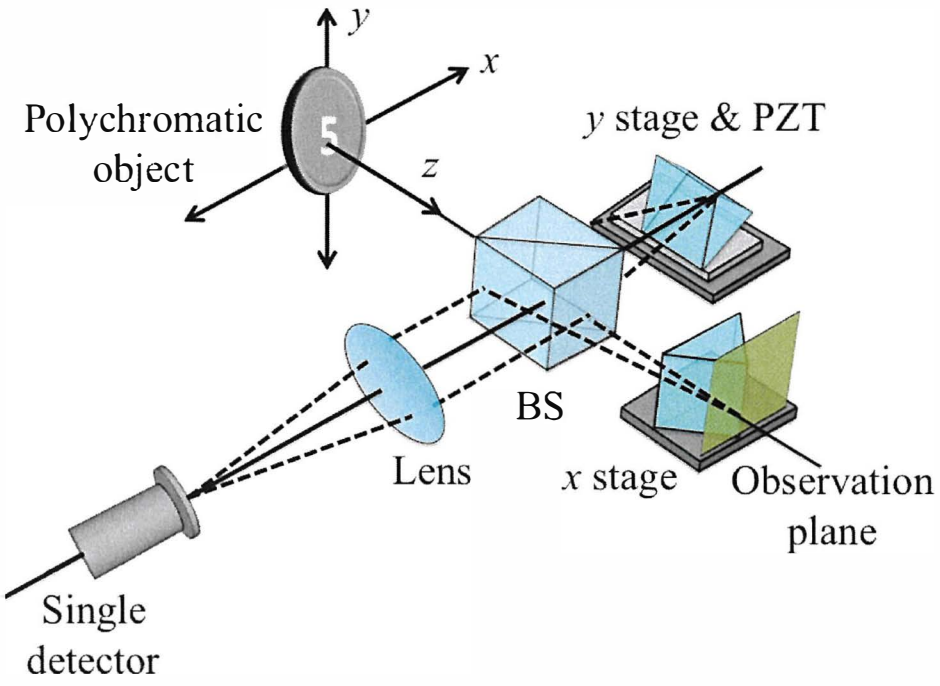

Fig. 4.1 Schematic diagram of experimental setup

This section demonstrates the experiment used to obtain the hyperbolic volume interferogram. The experimental setup is shown in Fig. 4.1. The measured object is a mask screen of the character "5" illuminated by a metal halide lamp (MHL) as a white light source, so that the object under measurement is a planar polychromatic object. Figure 4.2 shows the continuous spectral profile of the MHL as obtained by Fourier transform spectroscopy. The spectral resolution is 61.09 cm^{-1} and the spectral range is 3.13 $\times$ 10^4 cm^{-1}.

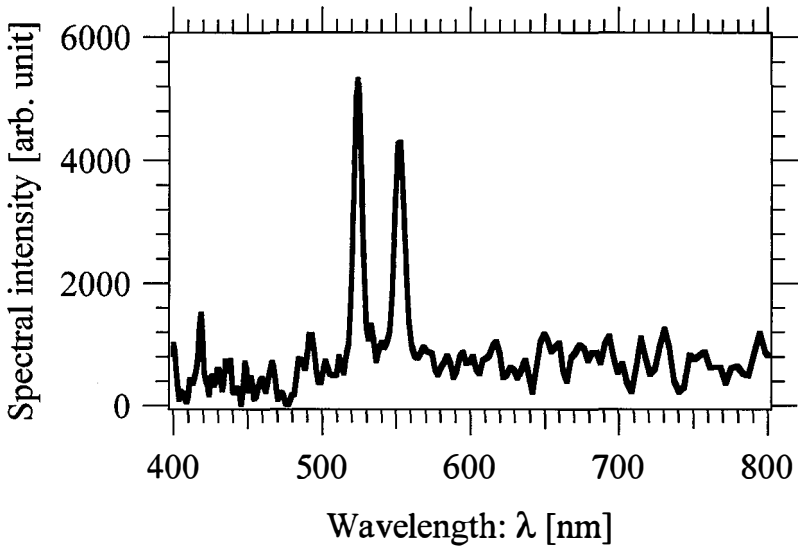

Fig. 4.2 Continuous spectral profile of the MHL as obtained by Fourier transform spectroscopy

Figure 4.3 shows a photograph of the illuminated mask screen, which has size 0.3 mm $\times$ 0.5 mm. The depth distance z of the object is measured from one of apex of prism P' to the origin of the Cartesian coordinate system (x,y) where the object is located. The depth is set at 115 mm or 135 mm. Light from the object propagates into the two-wavefront folding interferometer. The x and y stages are moved stepwise in intervals of 12.9 μm. The PZT is moved stepwise in the z direction in steps of 0.08 μm. From the number of movements of the stages and the PZT, the single detector records light intensities 262,144 (= 64 $\times$ 64 $\times$ 64) times.

Fig. 4.3 Photograph of the illuminated mask screen of the character "5"

4.3 Experimental results

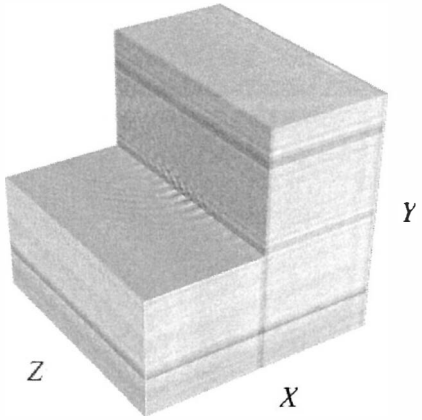

Fig. 4.4 Hyperbolic volume interferogram obtained by experiment

Figure 4.4 shows the hyperbolic volume interferogram obtained from the experiment. A quarter of the interferogram has been omitted to show the inner fringe arrangement. The lateral size of the recorded volume interferogram in the x and y directions is 825.6 μm and the thickness is 5.12 μm, respectively.

Figure 4.5 shows the continuous spectral profile of the object. This spectral profile is obtained by taking the Fourier transform along the center of the volume interferogram with respect to the thickness Z. In the figure, circles indicate the original data obtain from spectral channel of the Fourier transform. Thirteen points are shown, which covers the wavelength range of visible light.

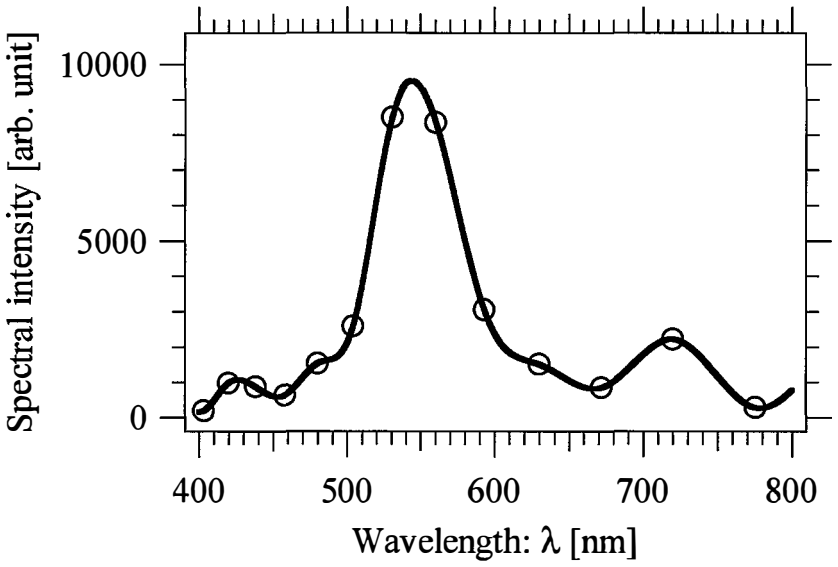

Fig. 4.5 Continuous spectral profile recorded on the observation plane by taking the Fourier transform along the center of the volume interferogram with respect to thickness *Z*.

The spectral resolution is limited by the step interval and number of steps for the PZT. In this experiment, a spectral occurs around 560 nm, as seen in Fig. 4.5, and the spectral resolution at this wavelength is 31.11 nm. This spectral profile agrees with that of the MHL to within the spectral resolution, as shown in Fig. 4.2. Thus, we will include the retrieved results at this spectral peak in what follows.

The panels in Fig. 4.6 show the phase distributions of the measured hyperbolic complex holograms (cross-spectral densities) at the spectral peak 560 nm with the object depth distance set at $z = 115$ mm and $z = 135$ mm. Figures 4.7(a) and 4.7(c) show the in-focus images that are retrieved from corresponding holograms over the *x*-*y* plane. Figures 4.7(b) and 4.7(d) show the intensity distribution over the *y*-*z* plane at $x = 0$. From Figs. 4.7(a) and 4.7(c), the images at the object depths are not correct for the measured object. The phase distributions in Fig. 4.6 may be distorted by phase aberration introduced by unintentional motions of the *x* and *y* stages. This is reflected in the image distortion in Fig. 4.7, with the correct image (the character "5") not retrieved. An in situ calibration method to eliminate this phase aberration will be presented in the next section.

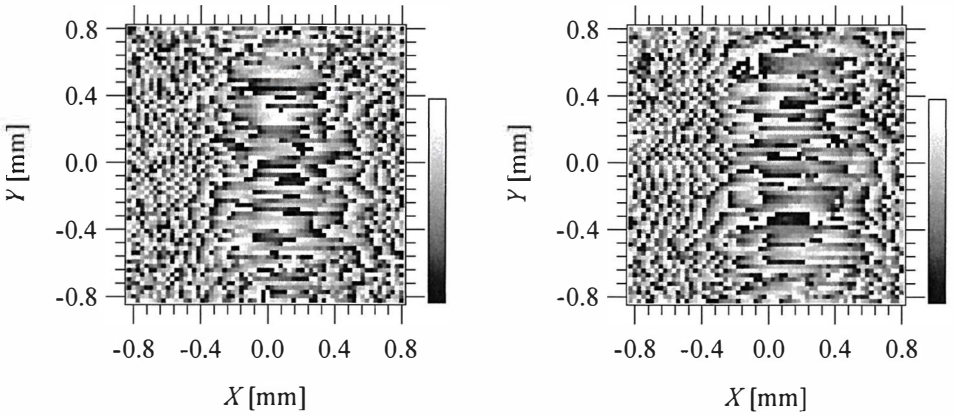

Fig. 4.6 Phase distribution of measured object at the spectral peak 560 nm and object depth distance of (a) $z = 115$ mm and (b) $z = 135$ mm.

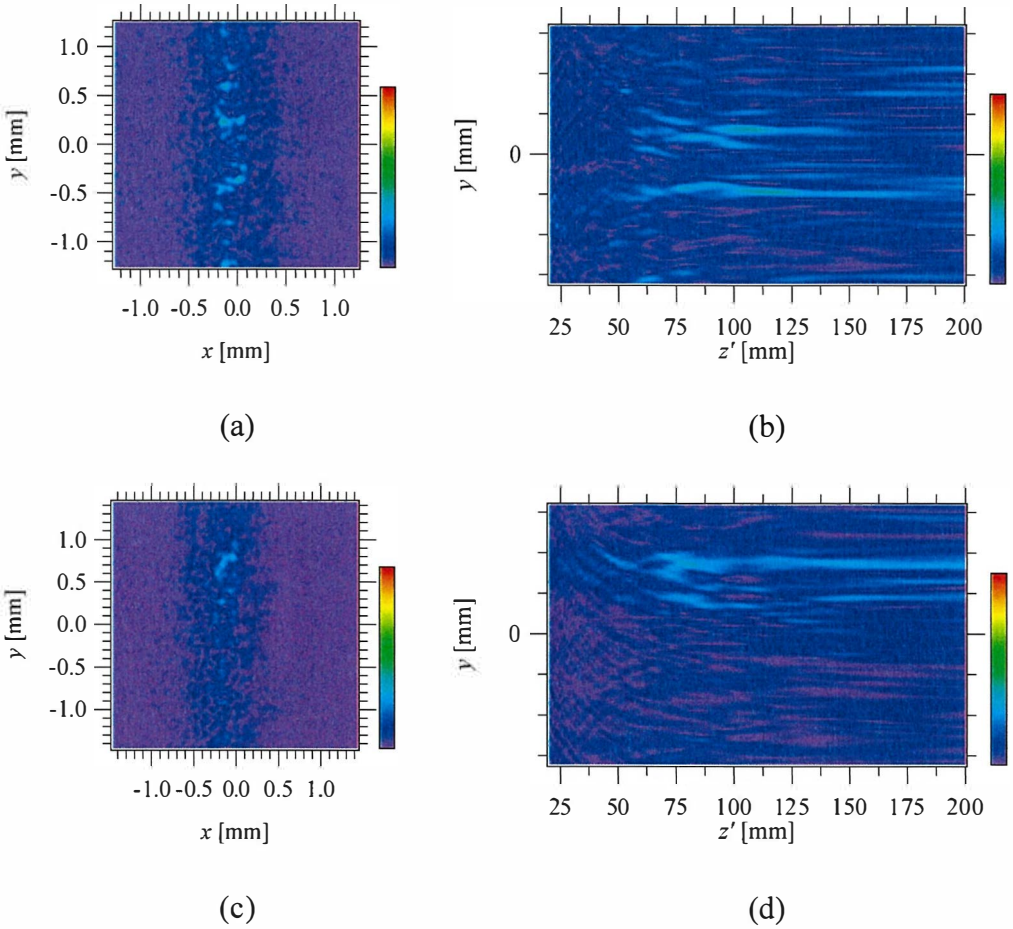

Fig. 4.7 The image retrieved for the measured object at $z = 115$ mm (a, b) and $z = 135$ mm (c, d). The in-focus image over the *x*-*y* plane at retrieval distances of (a) $z' = 115$ mm and (c) $z' = 140$ mm. The intensity distributions over the *y*-*z* plane are shown in (b) and (d).

4.4 In situ calibration method

Figures 4.7(a) and 4.7(b) show that the retrieved images are not correct. This can be explained by unintentional motion of the x and y stages during measurement of the volume interferogram, leading to changes in the phase distribution (i.e., phase aberration). In principle, the correct phase distribution for the hyperbolic hologram can be obtained by subtracting the phase aberration from the measured phase distribution.

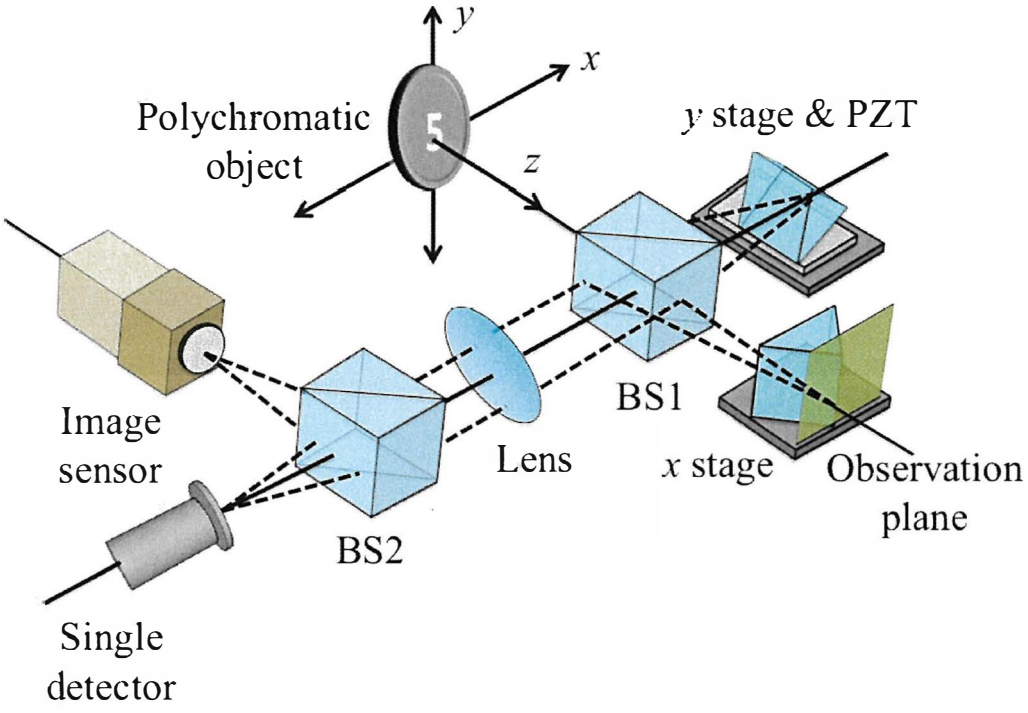

Fig. 4.8 Schematic diagram of an optical setup for in situ calibration

To calibrate for correction of this phase aberration, another BS and image sensor are inserted between the lens and single detector to perform simultaneous measurement of the volume interferogram, recording fringe patterns of the phase aberration only. Figure 4.8 shows a schematic diagram of an optical setup for this in situ calibration method. By choosing the pixel at $(x, y) = (X/2, Y/2)$ and arranging the pixel values according to the positions of the stages (X, Y, Z), another volume interferogram can be obtained in which a different spatial correlation function is recorded:

$$\Gamma(X/2, Y/2, z_0; X/2, Y/2, z_0 + Z) = \frac{1}{\lambda^2 z^2} \int S_\omega(\boldsymbol{r}_s) \exp(ikZ) d^3 r_s d\omega . \tag{4.1}$$

This spatial correlation function Eq. (4.1) contains an interference term related to only longitudinal shear. Drift in this shear results in phase aberration. Notably, it does not include a linear or quadratic phase factor, so it does not record the 3D information of the object. Given the motions of the x and y stages, if there is no drift of longitudinal shear between the two arms of the interferometer, the spatial correlation function in Eq. (4.1) is almost constant. However, when there is unintended motion of the x and y stages, phase aberration is introduced, and this spatial correlation function records it. The spectral decomposition of this spatial correlation function Γ gives a set of cross-spectral densities $W_\omega(X/2,Y/2;X/2,Y/2)$ that includes the information of the phase aberration at each spectral component. In this way, we may obtain phase aberration separately from the originally measured phase distribution.

In situ calibration to eliminate the phase aberration can be performed by subtracting the phase distribution of the cross-spectral density $W_\omega(X/2,Y/2;X/2,Y/2,z_0)$ from the phase distribution of the original cross-spectral density $W_\omega(X,0;0,Y,z_0)$. The phase aberration can be eliminated at each cross-spectral density (i.e., in the incoherent hyperbolic hologram) by this calibration.

Figure 4.9 shows the phase aberration of two experimental setups, with object depth distances of $z=115$ mm and $z=135$ mm. In both panels, the phase aberrations are almost the same. Thus, the phase aberration can be regarded as reproducible as long as the alignment of the interferometer does not change.

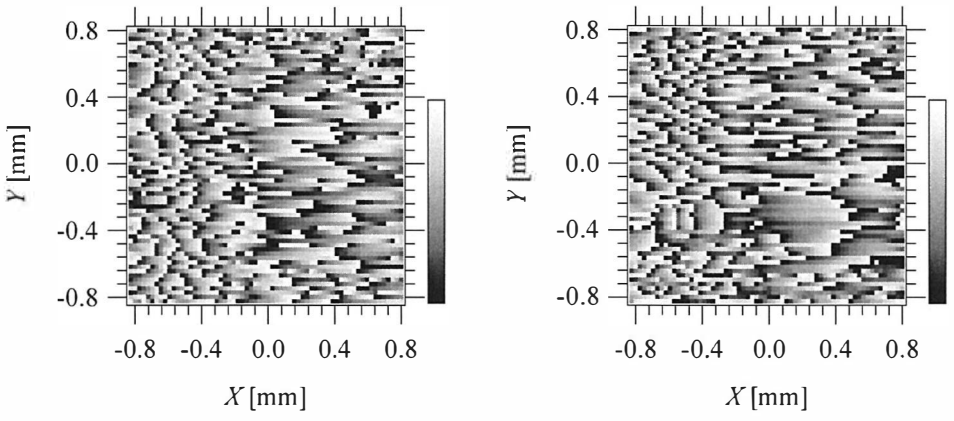

Fig. 4.9 Phase aberrations under two experimental conditions: object depth distances of (a) $z=115$ mm and (b) $z=135$ mm

4.5 Performance of calibration

The phase aberration of the experimental setup was corrected by the method presented in section 4.3. The calibrated phase distributions at the spectral peak (560 nm) of the measured object are shown for two experimental conditions in Fig. 4.10. From Fig. 4.10, a hyperbolic curve appears in the phase distributions.

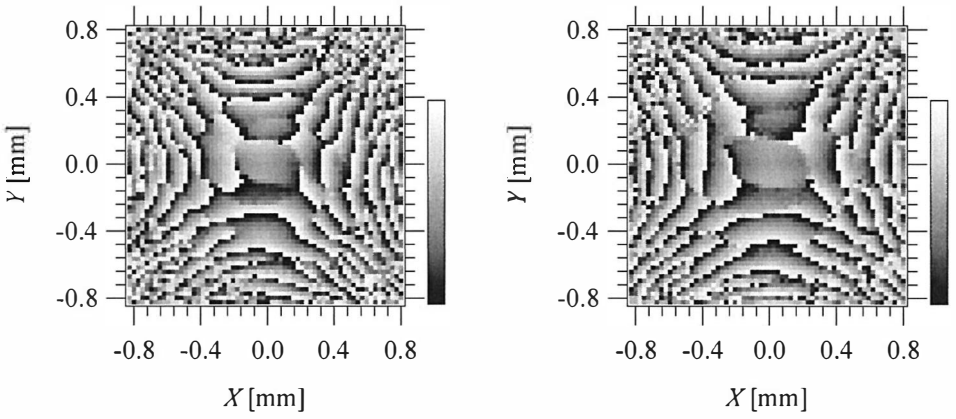

Fig. 4.10 Phase distribution of measured object after calibration to eliminate phase aberration at object depth distances of (a) $z = 115$ mm and (b) $z = 135$ mm

Figure 4.11(a) shows the in-focus image retrieved from the complex hologram shown in Fig. 4.10(a), where the object depth is $z = 115$ mm. From the intensity distribution of the in-focus image along the x and y axes, the dimensions of the retrieved object in Fig. 4.11(a) are 0.32 mm and 0.50 mm, respectively. These results agree well with the actual size of the measured object. Figure 4.11(b) shows the intensity distribution over the y-z plane at $x = 0$. The intensity peak appears close to the retrieved distance of $z' = 115$ mm.

Figure 4.11(c) shows the in-focus image retrieved from the complex hologram shown in Fig. 4.10(b), where the object depth is $z = 135$ mm. From the intensity distribution of the in-focus image along the x and y axes, the dimensions of the retrieved object in Fig. 4.11(c) are 0.34 mm and 0.52 mm, respectively. Here too, the results agree well with the actual size of the measured object. Figure 4.11(d) shows the intensity distribution over the y-z plane at $x = 0$. The intensity peak appears close to $z' = 140$ mm.

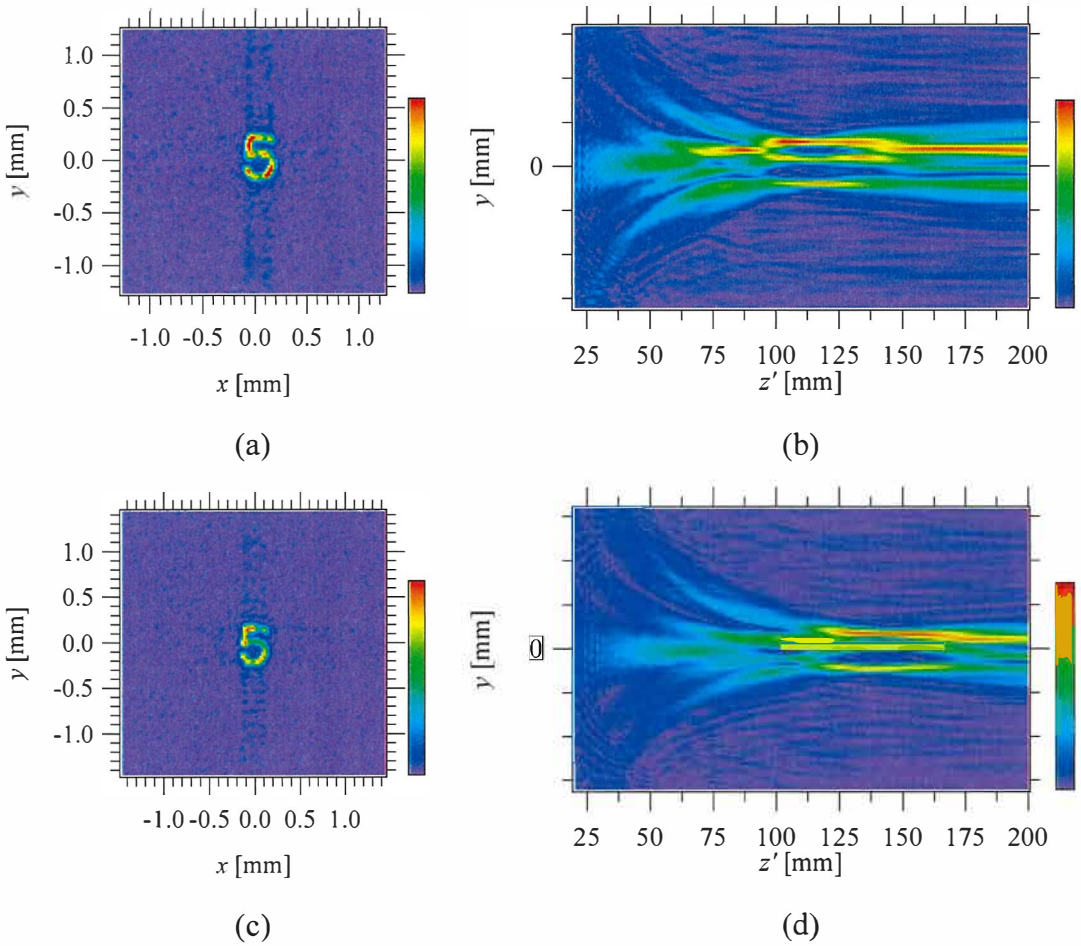

Fig. 4.11 Retrieved image after calibration for phase aberration when the measured object is located at $z = 115$ mm (a, b) and $z = 135$ mm (c, d). In-focus images over the x-y plane for retrieved distances of (a) $z' = 115$ mm and (c) $z' = 140$ mm. Intensity distribution over the y-z plane (b, d)

The retrieved distance and object depth are almost the same in both experimental results. Thus, the correct images can be retrieved by applying the phase calibration method, and the sizes of the retrieved object are almost the same as the size of the measured object. Although the measured object is a planar polychromatic object, a 3D image can obtain by changing the retrieval distance, as shown in Figs. 4.11(b) and (d).

4.6 Conclusion

Based on the two-wavefront folding interferometer, the hyperbolic volume interferogram can be measured directly. By Fourier transform of this volume interferogram with respect to the thickness Z, the spectral profile of the object and the phase distribution at each spectral component can be obtained. Because of the phase aberration that is included into the phase distribution, the retrieved image is not corrected, but the demonstrated in situ calibration method can separate the phase aberration from the phase distribution. This allows image reproducibility so long as the alignment of the interferometer does not change. After calibration, the correct phase distribution is obtained and retrieved image is correctly obtained. In the results shown here, the shape and size of the image agree well with the actual shape and size of the object.

V Mathematical analysis and comparison

5.1 Introduction

This section presents an investigation of the imaging properties of hyperbolic holography. The derivation of an analytical solution of the impulse response function (IRF) is presented. For the analytical solution, the object under investigations is a monochromatic point source represented by a 4D Dirac delta function. For experimental comparison, the object is a monochromatic point source realized by a He–Ne laser coupled with a fiber optic filament. The theoretical prediction from the analytical solution of the IRF is compared with the experimental results.

5.2 Analytical solution of impulse response function (IRF) of multispectral hyperbolic holography

To derive an analytical solution of the 4D IRF, we first assume that the object to be measured is a monochromatic point source with angular frequency $\omega_s = ck_s = 2\pi c/\lambda_s$. Here, the subscript s indicates that the parameters are source parameters (see Eq. (5.1)), and the spatial correlation function is measured along the x, y, and z axes within baseline lengths of l_x, l_y, and l_z, respectively (see Eq. (5.2)). We may write

$$S(x_s, y_s, z_s, \omega) = \delta^3(x_s - x_s', y_s - y_s', z_s - z_s')\delta(\omega - \omega_s), \tag{5.1}$$

$$A(X,Y,Z) = \text{rect}(X/l_x)\text{rect}(Y/l_y)\text{rect}(Z/l_z) = A(X,Y)\text{rect}(Z/l_z). \tag{5.2}$$

Here, $S(x_s, y_s, z_s, \omega)$ denotes the spectral density of the monochromatic point source and the 3D window function $A(X,Y,Z)$ specifies the size of the volume interferogram. This window function takes unit values in the measured area and zero outside.

Notice that, from Eq. (3.5), the cross-spectral density as actually measured across the observation plane is obtained by taking the Fourier transform of the 3D spatial correlation function $\Gamma(X, 0, z_0; 0, Y, z_0 + Z)$ with respect to the thickness Z. Then, the actually measured

cross-spectral density, denoted W_M, is expressed as a Fourier transform of the product of the window function A in Eq. (5.2) and the spatial correlation function Γ:

$$W_M(X,0,z_0;0,Y,z_0;\omega_i) = \frac{1}{2\pi c}\int A(X,Y,Z)\Gamma(X,0,z_0;0,Y,z_0+Z)\exp(-ik_iZ)dZ$$

$$= \frac{l_z}{2\pi}\mathrm{sinc}\left[\frac{l_z}{2}(k_s-k_i)\right]A(X,Y)W(X,0,z_0;0,Y,z_0;\omega_s), \tag{5.3}$$

where $\mathrm{sinc}\,x = (\sin x)/x$. The subscript i indicates that the parameters are used for the retrieval, and angular frequency for retrieval is $\omega_i = ck_i = 2\pi c/\lambda_i$. In Eq. (5.3), the product of the coefficient $l_z/2\pi$ and the sinc function represents the spectral IRF determined by the limited baseline length l_z. The actually measured cross-spectral density W_M is extended within the width of the spectral IRF.

For the next step, we obtain the 3D object information from the cross-spectral density. With the 2-FT method, the cross-spectral density $W_M(X,0,z_0;0,Y,z_0;\omega_i)$ is converted to the angular cross-spectral density $\tilde{W}_M(k_x,0,z_0;0,k_y,z_0;\omega_i)$. Then, it is multiplied by the OTF to produce $\tilde{W}_M(k_x,0,z_0-z';0,k_y,z_0-z';\omega_i)$, and inverse conversion gives the cross-spectral density $W_M(X,0,z_0-z';0,Y,z_0-z';\omega_i)$. Therefore, the finally obtained cross-spectral density is expressed as

$$W_M(X,0,z_0-z';0,Y,z_0-z';\omega_i) = \frac{\lambda_i z_i}{4\pi^2}\int W_M(X,0,z_0;0,Y,z_0;\omega_i)$$

$$\times\exp\left\{i\left[(X-x_i)k_{ix}-(Y-y_i)k_{iy}\right]+i\frac{z_i}{2k_i}(-k_{ix}^2+k_{iy}^2)\right\}dk_{ix}dk_{iy}dXdY. \tag{5.4}$$

The cross-spectral density $W_M(X,0,z_0-z';0,Y,z_0-z';\omega_i)$ is proportional to the spectral density $S'(x_s,y_s,z_s)$ at a source plane. Thus, the retrieved 3D image $O(x_i,y_i,z_i,\omega_i)$ is rewritten, after a straightforward but lengthy calculation, as

$$O(x_i, y_i, z_i, \omega_i)$$
$$= \frac{l_z}{2\pi\lambda_s^2 z^2}\operatorname{sinc}\left[\frac{l_z}{2}(k_s - k_i)\right]\exp\left[-i\frac{k_i}{2z_i}(-x_i^2 + y_i^2)\right]$$
$$\times \int_{-l_x/2}^{l_x/2}\exp\left[i\frac{k_i}{z_i}(mx_s - x_i)X\right]\exp\left[-i\frac{k_i}{2z_i}(m-1)X^2\right]dX$$
$$\times \int_{-l_y/2}^{l_y/2}\exp\left[-i\frac{k_i}{z_i}(my_s - y_i)Y\right]\exp\left[i\frac{k_i}{2z_i}(m-1)Y^2\right]dY. \quad (5.5)$$

Here, $m = k_s z_i/(k_i z) = \lambda_i z_i/(\lambda_s z)$ denotes the magnification, representing the ratio of the product of the wavelength and the depth of the object and retrieved image. Because in the linear-optical system, the output image is represented by the superposition integral of the input image and IRF, we have:

$$O(x_i, y_i, z_i, \omega_i) = \int S(x_s, y_s, z_s, \omega)h(x_i, y_i, z_i, \omega_i; x_s, y_s, z_s, \omega_s)d^3r_s d\omega. \quad (5.6)$$

To calculate the 4D IRF, we begin by consider the right-hand side of Eq. (5.6). Using Eq. (5.1) and applying the sifting property of delta function, we may express this as

$$h(x_i,y_i,z_i,\omega_i;x_s,y_s,z_s,\omega_s) = \int \delta^3(x_s - x_s', y_s - y_s', z_s - z_s')\delta(\omega - \omega_s)$$
$$\times h(x_i,y_i,z_i,\omega_i;x_s,y_s,z_s,\omega_s)d^3r_s d\omega. \quad (5.7)$$

Next, consider Eq. (5.5), the integral term of which may be classified into three cases as follows.

Case 1: Magnification $m = 1$, that is, $\lambda_i z_i = \lambda_s z$

In this case, Eq. (5.5) is expressed as in the following form after simple calculation:

$$O(x_i, y_i, z_i, \omega_i)$$
$$= \frac{l_x l_y l_z}{2\pi\lambda_s^2 z^2}\exp\left[-i\frac{k_i}{2z_i}(-x_i^2 + y_i^2)\right]$$
$$\times \operatorname{sinc}\left[\frac{l_z}{2}(k_s - k_i)\right]\operatorname{sinc}\left[\frac{l_x k_i}{2z_i}(x_s - x_i)\right]\operatorname{sinc}\left[\frac{l_y k_i}{2z_i}(y_s - y_i)\right]. \quad (5.8)$$

Case 2: Magnification $m \neq 1$, $0 < m < 1$, that is, $\lambda_i z_i \neq \lambda_s z$

In this case, $m - 1 = -|m - 1|$, and the integral term in Eq. (5.5) is transformed to a perfect

square expression:

$$
\begin{aligned}
&O(x_i, y_i, z_i, \omega_i) \\
&= \frac{l_z}{2\pi\lambda_s^{\,2} z^2}\operatorname{sinc}\left[\frac{l_z}{2}(k_s - k_i)\right]\exp\left[-i\frac{k_i}{2z_i}(-x_i^{\,2} + y_i^{\,2})\right] \\
&\times \int_{-l_x/2}^{l_x/2}\exp\left\{-i\frac{k_i}{2z_i}(m-1)\left[X - \frac{(mx_s - x_i)}{m-1}\right]^2\right\}\left\{\exp\left[i\frac{k_i}{2z_i}\frac{(mx_s - x_i)^2}{m-1}\right]\right\}dX \\
&\times \int_{-l_y/2}^{l_y/2}\exp\left\{i\frac{k_i}{2z_i}(m-1)\left[Y - \frac{(my_s - y_i)}{m-1}\right]^2\right\}\left\{\exp\left[-i\frac{k_i}{2z_i}\frac{(my_s - y_i)^2}{m-1}\right]\right\}dY. \qquad (5.9)
\end{aligned}
$$

Here, we introduce new parameters τ_x and τ_y that are expressed a

$$
\sqrt{\frac{\pi}{2}}\tau_x = \sqrt{\frac{k_i(m-1)}{2z_i}}\left[X - \frac{(mx_s - x_i)}{m-1}\right] \qquad (5.10)
$$

$$
\sqrt{\frac{\pi}{2}}\tau_y = \sqrt{\frac{k_i(m-1)}{2z_i}}\left[Y - \frac{(my_s - y_i)}{m-1}\right]. \qquad (5.11)
$$

Substituting Eqs. (5.10) and Eq. (5.11) into Eq. (5.9) yields

$$
\begin{aligned}
&O(x_i, y_i, z_i, \omega_i) \\
&= \frac{l_z}{2\pi\lambda_s^{\,2} z^2}\operatorname{sinc}\left[\frac{l_z}{2}(k_s - k_i)\right]\exp\left[-i\frac{k_i}{2z_i}(-x_i^{\,2} + y_i^{\,2})\right] \\
&\times i\sqrt{\frac{\pi z_i}{k_i|m-1|}}\exp\left[i\frac{k_i}{2z_i}\frac{(mx_s - x_i)^2}{m-1}\right]\int_{i\alpha^-}^{i\alpha^+}\exp\left(-i\frac{\pi}{2}\tau_x^{\,2}\right)d\tau_x \\
&\times i\sqrt{\frac{\pi z_i}{k_i|m-1|}}\exp\left[-i\frac{k_i}{2z_i}\frac{(my_s - y_i)^2}{m-1}\right]\int_{i\beta^-}^{i\beta^+}\exp\left(i\frac{\pi}{2}\tau_y^{\,2}\right)d\tau_y, \qquad (5.12)
\end{aligned}
$$

where

$$
\alpha^{\pm} = \sqrt{\frac{k_i\,|m-1|}{\pi z_i}}\left(\pm\frac{l_x}{2} - \frac{mx_s - x_i}{m-1}\right), \qquad (5.13)
$$

$$
\beta^{\pm} = \sqrt{\frac{k_i\,|m-1|}{\pi z_i}}\left(\pm\frac{l_y}{2} - \frac{my_s - y_i}{m-1}\right). \qquad (5.14)
$$

Consider the integral with respect to τ_x in Eq. (5.12). It is represented as the following formula using the Fresnel integrals $\mathbf{C}(a)$ and $\mathbf{S}(a)$.

$$
\int_{i\alpha^-}^{i\alpha^+}\exp\left(-i\frac{\pi}{2}\tau_x^{\,2}\right)d\tau_x = \left\{\mathbf{C}(i\alpha^+) - \mathbf{S}(i\alpha^+)i\right\} - \left\{\mathbf{C}(i\alpha^-) - \mathbf{S}(i\alpha^-)i\right\}
$$

$$= i\sqrt{2}\exp(i\frac{\pi}{4})\left\{\mathbf{F}(\alpha^{+}) - \mathbf{F}(\alpha^{-})\right\} \tag{5.15}$$

Here,

$$\mathbf{C}(a) = \int_0^a \cos\left(\frac{\pi}{2}\tau^2\right)d\tau, \tag{5.16}$$

$$\mathbf{S}(a) = \int_0^a \sin\left(\frac{\pi}{2}\tau^2\right)d\tau, \tag{5.17}$$

and the function $\mathbf{F}(a)$ is defined as in Eq. (5.18)[8] in terms of the real component of $\mathbf{C}(a)$ and the imaginary component of $\mathbf{S}(a)$[9].

$$\mathbf{F}(a) = \frac{1}{\sqrt{2}}\exp\left(-i\frac{\pi}{4}\right)\left\{\frac{1}{2} + \mathbf{C}(a) + i\left[\frac{1}{2} + \mathbf{S}(a)\right]\right\} \tag{5.18}$$

Substituting Eq. (5.15) into Eq. (5.12) and then using a similar procedure for the integral with respect to τ_y, the analytical solution of the cross-spectral density can be written in the following form:

$$\begin{aligned} &O(x_i, y_i, z_i, \omega_i) \\ &\quad = \frac{l_z}{2\pi\lambda_s^{\,2} z^2}\operatorname{sinc}\left[\frac{l_z}{2}(k_s - k_i)\right]\exp\left[-i\frac{k_i}{2z_i}(-x_i^{\,2} + y_i^{\,2})\right] \\ &\quad \times \frac{\pi z_i}{k_i|m-1|}\exp\left\{i\frac{k_i}{2z_i|m-1|}\left[-(mx_s - x_i)^2 + (my_s - y_i)^2\right]\right\} \\ &\quad \times 2\left\{\mathbf{F}(\alpha^{+}) - \mathbf{F}(\alpha^{-})\right\}\left\{\mathbf{F}^{*}(\beta^{+}) - \mathbf{F}^{*}(\beta^{-})\right\}. \end{aligned} \tag{5.19}$$

Case 3: Magnification $m \neq 1$, $m > 1$, that is, $\lambda_i z_i \neq \lambda_s z$

In this case, $m - 1 = |m-1|$, Eq. (5.12) is represented as

$$\begin{aligned} &O(x_i, y_i, z_i, \omega_i) \\ &\quad = \frac{l_z}{2\pi\lambda_s^{\,2} z^2}\operatorname{sinc}\left[\frac{l_z}{2}(k_s - k_i)\right]\exp\left[-i\frac{k_i}{2z_i}(-x_i^{\,2} + y_i^{\,2})\right] \\ &\quad \times \sqrt{\frac{\pi z_i}{k_i|m-1|}}\exp\left[i\frac{k_i}{2z_i}\frac{(mx_s - x_i)^2}{m-1}\right]\int_{\alpha^{-}}^{\alpha^{+}}\exp\left(-i\frac{\pi}{2}\tau_x^{\,2}\right)d\tau_x \\ &\quad \times \sqrt{\frac{\pi z_i}{k_i|m-1|}}\exp\left[-i\frac{k_i}{2z_i}\frac{(my_s - y_i)^2}{m-1}\right]\int_{\beta^{-}}^{\beta^{+}}\exp\left(i\frac{\pi}{2}\tau_y^{\,2}\right)d\tau_y. \end{aligned} \tag{5.20}$$

The integral with respect to τ_x in Eq. (5.20) is represented by the following formula:

$$\int_{\alpha^-}^{\alpha^+} \exp\left(-i\frac{\pi}{2}\tau_x{}^2\right)d\tau_x = \left\{\mathbf{C}(\alpha^+) - i\mathbf{S}(\alpha^+)\right\} - \left\{\mathbf{C}(\alpha^-) - i\mathbf{S}(\alpha^-)\right\}$$

$$= \sqrt{2}\exp(-i\frac{\pi}{4})\left\{\mathbf{F}^*(\alpha^+) - \mathbf{F}^*(\alpha^-)\right\}. \tag{5.21}$$

Therefore, Eq. (5.20) can be expressed as

$$\begin{aligned} &O(x_i, y_i, z_i, \omega_i) \\ &= \frac{l_z}{2\pi\lambda_s{}^2 z^2}\mathrm{sinc}\left[\frac{l_z}{2}(k_s - k_i)\right]\exp\left[-i\frac{k_i}{2z_i}(-x_i{}^2 + y_i{}^2)\right] \\ &\times \frac{\pi z_i}{k_i|m-1|}\exp\left\{-i\frac{k_i}{2z_i|m-1|}\left[-(mx_s - x_i)^2 + (my_s - y_i)^2\right]\right\} \\ &\times 2\left\{\mathbf{F}^*(\alpha^+) - \mathbf{F}^*(\alpha^-)\right\}\left\{\mathbf{F}(\beta^+) - \mathbf{F}(\beta^-)\right\}. \end{aligned} \tag{5.22}$$

Therefore, using Eqs. (5.7), (5.8), (5.19), and (5.22), the final expression of the 4D IRF as found by the proposed method is written

$$\begin{aligned} &h(x_i, y_i, z_i, \omega_i; x_s, y_s, z_s, \omega_s) \\ &= \frac{ml_z}{2\pi c\lambda_s z|m-1|}\mathrm{sinc}\left[\frac{l_z}{2}(k_s - k_i)\right]\exp\left[-i\frac{k_i}{2z_i}(-x_i^2 + y_i^2)\right] \\ &\times \exp^{(*)}\left\{-i\frac{k_i}{2z_i|m-1|}\left[-(mx_s - x_i)^2 + (my_s - y_i)^2\right]\right\} \\ &\times \left\{\left[\mathbf{F}^*(\alpha^+) - \mathbf{F}^*(\alpha^-)\right]\left[\mathbf{F}(\beta^+) - \mathbf{F}(\beta^-)\right]\right\}^{(*)}, \end{aligned} \tag{5.23}$$

where the complex conjugation, marked (*), appear only if $0 < m < 1$. In Eq. (5.23), if we take the limit as $m \to 1$, then Eq. (5.23) reduces to

$$\begin{aligned} &h(x_i, y_i, z_i, \omega_i; x_s, y_s, z_s, \omega_s) \\ &= \frac{l_x l_y l_z}{2\pi\lambda_s{}^2 z^2}\exp\left[-i\frac{k_i}{2z_i}(-x_i^2 + y_i^2)\right] \\ &\times \mathrm{sinc}\left[\frac{l_z}{2}(k_s - k_i)\right]\mathrm{sinc}\left[\frac{l_x k_i}{2z_i}(x_s - x_i)\right]\mathrm{sinc}\left[\frac{l_y k_i}{2z_i}(y_s - y_i)\right]. \end{aligned} \tag{5.24}$$

This function corresponds to the diffraction-limited in-focus image of the monochromatic point source.

Equation (5.23) is the 4D IRF given by the proposed method and is defined over (x, y, z, ω) space. Equation (5.24) corresponds to the diffraction-limited in-focus image of the monochromatic point source. As was previously suggested for the IRF of the spherical-type (S-type) method[7], the recorded fringe patterns of the S-type method correspond directly to the phase distributions of the wavefront of the many spectral components propagated from the object being measured. Accordingly, the complex holograms derived from an S-type method correspond to the ordinary phase distribution as obtained by inline phase-shifting holography.

In hyperbolic holography, the recorded fringe patterns do not correspond simply to the wavefront propagated from the object. However, these analytical solutions of the 4D IRF in this method have a mathematical form similar to the solutions from the S-type method. In particular, the diffraction-limited in-focus image is consistent except for differences in the coefficients. These differences are caused by the retrieval process. In the analytical solution of the S-type method, the convolution integral is directly calculated. In contrast, the analytical solution for hyperbolic holography is calculated by a Fourier transform and inverse Fourier transform. Therefore, although the recorded fringe patterns do not correspond simply to the wavefront propagated from the object, the spectral resolution and spatial resolution are determined in the same manner as with the S-type method.

5.3 Comparison of properties predicted by IRF and obtained by experiment

In an experiment to validate the IRF, a monochromatic point source composed of optical fiber and a He–Ne laser with wavelength 543.5 nm is measured. This source is located near the origin of the coordinate system. The object depth distance is 67 mm. Light propagates through the two-wavefront folding interferometer. Prisms P and P' were moved stepwise (32 steps each, with interval 12.9 μm). The PZT was also moved stepwise (64 steps, with an interval 0.08 μm).

The spectral profile obtained from volume interferogram is shown in Fig. 5.1. The intensity peak is located around 531 nm. This agrees well with the wavelength of He–Ne

lasers, to within the spectral resolution. Next, the experimental and analytical results will be compared.

Figure 5.2 shows the phase distribution of each cross-spectral density at the spectral peak 531 nm. Figure 5.2(a) shows the phase distribution of the cross-spectral densities at the spectral peak that appeared in Fig. 5.1. This is an uncorrected cross-spectral density that includes the phase aberration. Figure 5.2(b) shows the distribution of the phase aberration at the spectral peak obtained after applying the calibration method proposed in section 4.4. Figure 5.2(c) shows the phase distribution of the cross-spectral density (after calibration). Figure 5.2(d) shows the theoretical phase distributions of the cross-spectral density in this experiment as calculated from the analytical solution of the 4D IRF.

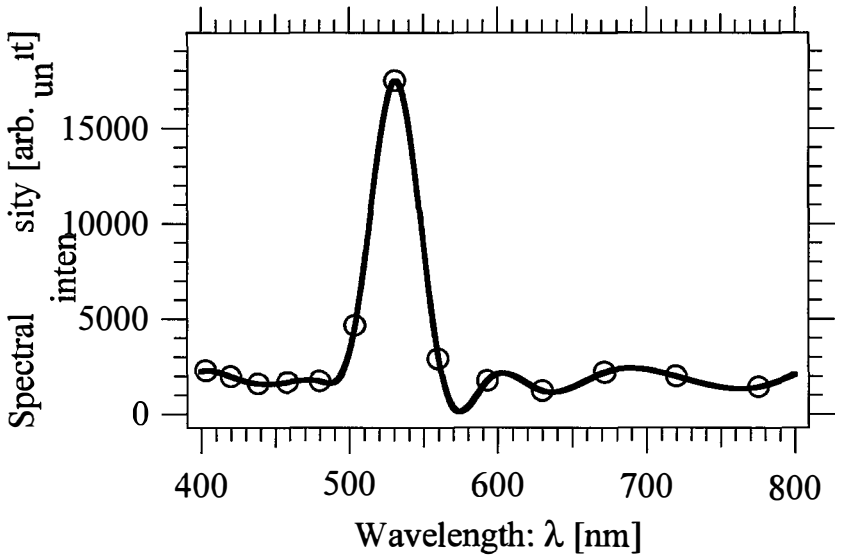

Fig. 5.1 Spectral profile obtained from volume interferogram. The measured object is a monochromatic point source with wavelength 543.5 nm

In Fig. 5.2(a), the phase distribution is not a hyperbolic curve because it contains the phase aberration. After calibration, we obtain the phase distribution as a hyperbolic curve, which is shown in Fig. 5.2(c). Comparison between the calibrated phase distributions in Fig. 5.2(c), which was obtained by experiment, and the phase distribution in Fig. 5.2(d), which was obtained by analytical solution of the 4D IRF, shows good agreement. Thus, we can see that the phase aberration is largely eliminated by the proposed calibration method.

Figures 5.3 shows the in-focus image over the x-y plane at $\lambda = 531$ nm retrieved from distance $z' = 67$ mm. Figure 5.3(a) is obtained from the original phase distribution, Fig.

5.3(b) is obtained from the phase distributions after calibration, and Fig. 5.3(c) is calculated from the analytical solution of 4D IRF in Eq. (5.23). In Fig. 5.3(a), the image is blurry and we cannot retrieve the image of the point source. After calibration, we can retrieve the correct image, as seen in Fig. 5.3(b). Comparing between the retrieved images in Fig. 5.3(b), which was obtained by experiment, and the retrieved image in Fig. 5.3(c), which was obtained by analytical solution of the 4D IRF, we find that these are also in good agreement.

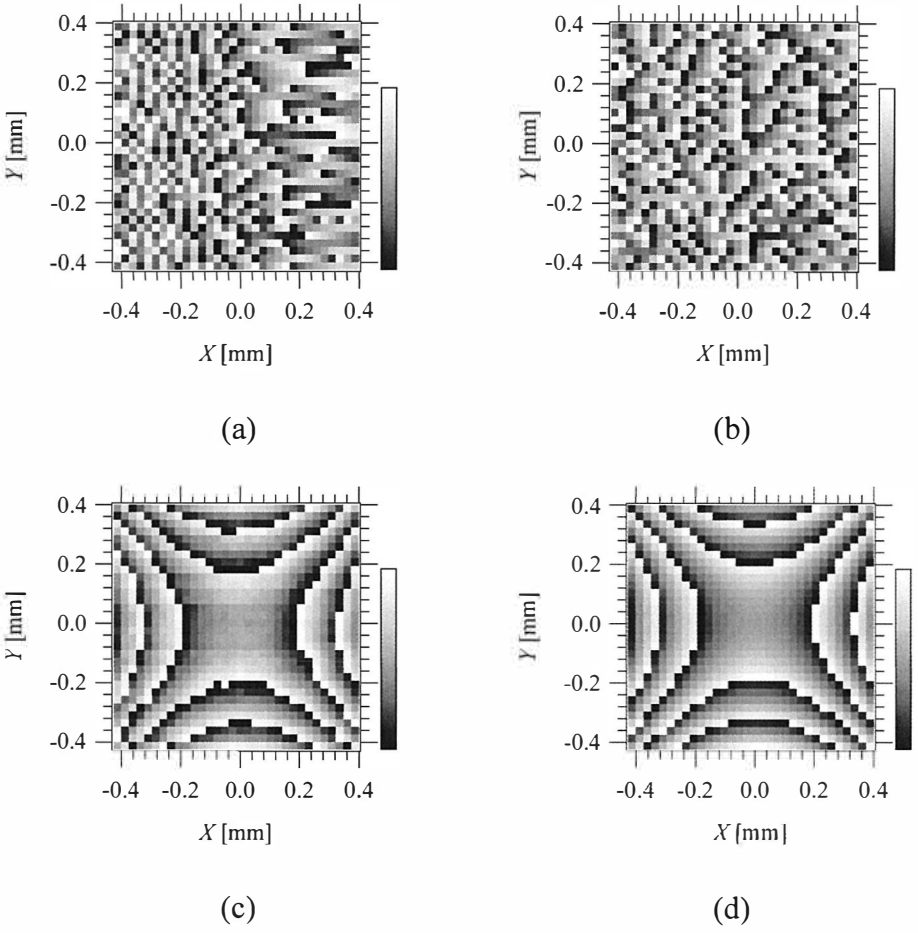

Fig. 5.2 (a) Phase distributions of the cross-spectral densities at the spectral peak appearing in Fig. 5.1. (b) Phase aberration distributions at the spectral peak recovered from the other cross-spectral densities. (c) Phase distributions of the cross-spectral density after calibration. (d) Theoretically derived phase distributions of the cross-spectral density in the experimental conditions

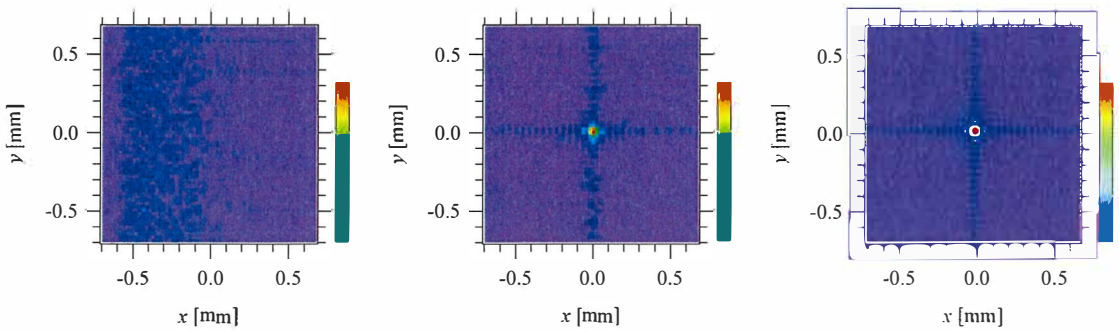

Fig. 5.3 In-focus image over x-y plane at $\lambda = 531$ nm from distance $z' = 67$ mm. Each image is obtained from (a) the original phase distributions shown in Fig. 5.2(a); (b) phase distributions after calibration (see Fig. 5.2(c)); and (c) analytical solution of the 4D IRF (Eq. (5.23)).

Figure 5.4 shows the intensity distributions over the x-z plane. Figure 5.4(a) is obtained from the original phase distribution, Fig. 5.4(b) is obtained from the phase distribution after calibration, and Fig. 5.4(c) is calculated from the analytical solution of the 4D IRF in Eq. (5.23). Comparing between the experimental result shown in Fig. 5.4(b) and the theoretical prediction shown in Fig. 5.4(c), we find that the intensity peak is located at the same position, and the spreads in the longitudinal direction also agree well. Finally, details can be clearly seen from the next figure. Figure 5.5 shows a comparison of the intensity profiles of the retrieved images along the z axis. In this, the original phase distributions are shown with a dashed curve, the calibrated phase distributions with a dotted curve, and the theoretical prediction with a solid curve.

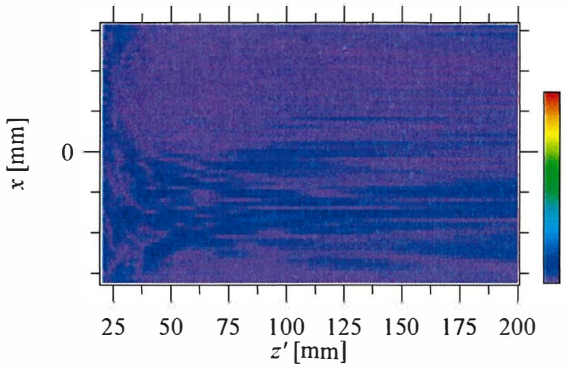

(a)

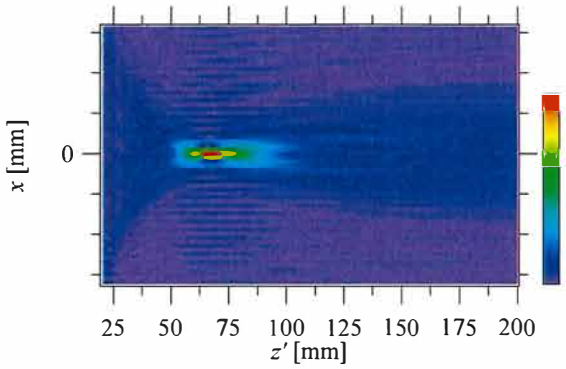

(b)

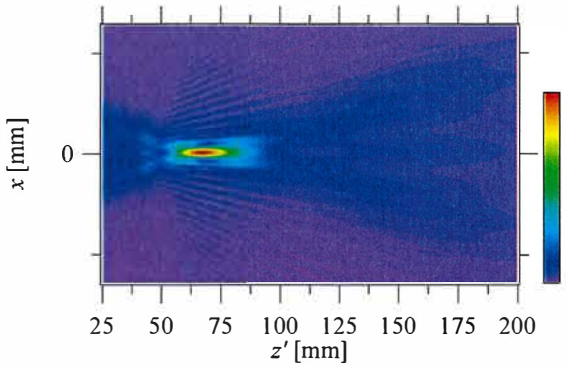

(c)

Fig. 5.4 Intensity distribution over the *x*-*z* plane. The images are obtained from (a) the original phase distributions shown in Fig. 5.2(a); (b) the phase distributions after calibration; and (c) the analytical solution of the 4D IRF.

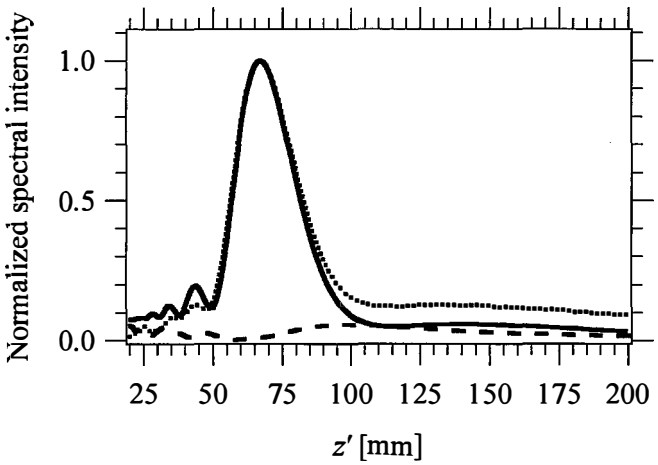

Fig. 5.5 Comparison of intensity profiles of retrieved images along *z*-axis. The patterns are as follows: original phase distributions, dashed curve; phase distributions after calibration, dotted curve; analytical solution of the 4D IRF, solid curve.

5.4 Conclusion

From an analytical solution of the IRF of multispectral hyperbolic holography, it is shown that the spectral resolution and spatial resolution can be determined. From Fig. 5.5, the curves calculated by the analytical solution of the 4D IRF agree well with experimental results. Overall, the results obtained from application of the phase calibration method enable retrieving correct 3D information for a measured object, and the 4D IRF gives the correct spectral resolution and 3D spatial resolution for multispectral hyperbolic digital holography.

VI Conclusions

In this dissertation, I proposed a new method for obtaining multispectral 3D images. In this method, a hyperbolic volume interferogram is directly measured by an appropriately designed interferometer. In this interferometer, only the intensity on the optical axis is measured, so it can use a single detector that has higher sensitivity and higher dynamic range than image sensors. This makes it possible to achieve a highly sensitive interferometric system. However, a phase aberration occurs during measurement. To address this, I proposed a calibration method that corrects the phase distribution. Basically, the measured interferogram is affected primarily by a drift in path difference caused by misalignment and unwanted motion of the stages. The phase aberrations are then included in the interferogram. Instead, the phase aberration caused by these factors can be obtained separately by a one-time in situ experiment. Moreover, I investigated the imaging properties of multispectral hyperbolic incoherent holography based on a novel analytical solution of an IRF defined over a 4D space.

In the work, it is shown that the spectral resolution and 3D imaging properties obtained experimentally by applying the in situ calibration method agree well with the properties theoretically predicted from the novel 4D IRF. I also found that the spectral resolution and 3D spatial resolutions could be determined in the same manner as with ordinary coherent holography. In general, because of the advanced features of this method, it is expected to have wider application and offer a higher dynamic range for an interferometric system than conventional works in this branch of research. In the proposed method, the measurement time is not a concern. The method can be applied to investigation of the refractive index distribution or local spectral distribution of opaque objects. In future work, it may be possible to reduce the measurement time by using a mirror galvanometer system instead of a setup in which system movement is synchronized to the recording timing of the single detector.

Acknowledgements

First, I express my sincere gratitude to my supervisor Assoc. Prof. Kyu Yoshimori for his continuous support of my Ph.D work and related research. His guidance has helped me throughout my research and the writing of this dissertation.

In addition to my advisor, I thank Assist. Prof. Prathan Buranasiri and Dr. Witoon Yindeesuk, who provided me an opportunity to meet my advisor. Without their precious support, it would not have been possible to conduct this research.

I thank my fellow lab mates for stimulating discussions, for our time working together, and for all the activity we have had in the last three years. In particular, I am grateful to Dr. Masaki Obara for enlightening me from my first experiences of research. Last, but not least, I thank my family: my parents, my wife, my daughter, and my son for supporting me spiritually throughout the process of writing this dissertation and in my life in general.

References

1) M. Sasamoto and K. Yoshimori, "Three-dimensional Imaging Spectrometry by fully passive interferometry," Opt. Rev. **19** (2012) 29.
2) S. Teeranutranont and K. Yoshimori, "Digital holographic three-dimensional imaging spectrometry," Appl. Opt. **52** (2013) A388.
3) T. Hashimoto, A. Hirai, and K. Yoshimori, "Fully interferometric three-dimensional imaging spectrometry using hyperbolic-type volume interferogram," Appl. Opt. **52** (2013) 1497.
4) M. Obara and K. Yoshimori, "Coherence Three-Dimensional Imaging Spectrometry Based on Measurement of Rotated-Hyperbolic Volume Interferograms," Opt. Rev. **21** (2014) 479.
5) M. Obara and K. Yoshimori, "Systematic study of synthetic aperture processing in interferometric three-dimensional image spectrometry," Jpn. J. Appl. Phys. **56** (2017) 022402.
6) K. Srinuanjan, M. Obara and K. Yoshimori, "Multispectral hyperbolic incoherent holography," Opt. Rev. **25** (2018) 65.
7) M. Obara and K. Yoshimori, "3D spatial resolution and spectral resolution of interferometric 3D imaging spectrometry," Appl. Opt. **55** (2016) 2489.
8) K. Yoshimori, A. Hirai, T. Inoue, K. Itoh, and Y. Ichioka, "Effects of a linear edge on optical imaging" J. Opt. Soc. Am. A **12** (1995) 981.
9) *Handbook of Mathematical Functions with Formulas, Graphs, and Mathematic Tables*, ed. M. Abramowitz and I. Stegun (Dover Publications, Inc., New York, 1970), 9th ed., p. 300.
10) P. Xia, Y. Awatsuji, K. Nishio, S. Ura, and O. Matoba, "Parallel phase-shifting digital holography using spectral estimation technique," Appl. Opt. **53** (2014) G123.
11) J. W. Goodman: *Introduction to Fourier Optics* (McGraw-Hill, New York, 1996) 2nd ed., p. 369.
12) J. Rosen and G. Brooker, "Digital spatially incoherent Fresnel holography," Opt. Lett. **32** (2007) 912.
13) G. Brooker, N. Siegel, V. Wang, and J. Rosen, "Optimal resolution in Fresnel incoherent correlation holographic fluorescence microscopy," Opt. Express **19** (2011) 5047.
14) A. Vijayakumar, Y. Kashter, R. Kelner, and J.Rosen, "Coded aperture correlation holography-a new type of incoherent digital holograms," Opt. Express **24** (2016) 12430.
15) M. K. Kim, "Incoherent digital holographic adaptive optics," Appl. Opt. **52** (2013) A117.

16) D. N. Naik, G. Pedrini, M. Takeda, and W. Osten, "Spectrally resolved incoherent holography: 3D spatial and spectral imaging using a Mach-Zehnder radial-shearing interferometer," Opt. Lett. **39** (2014) 1857.
17) K. Watanabe and T. Nomura, "Recording spatially incoherent Fourier hologram using dual channel rotational shearing interferometer," Appl. Opt. **54** (2015) A18.

Appendix: Derivation of equations (3.6) and (3.10)

Consider the relationship between the spectral density $S(x_s, y_s, z_s)$ at light source plane and the cross-spectral density $W(X, 0, z_0; 0, Y, z_0)$ at the observation plane. The angular frequency ω is suppressed because the light source is considered as a monochromatic component of the optical field. The spectral density $S(x_s, y_s, z_s)$ is first expressed in the following form:

$$S(x_s, y_s, z_s) = \langle U_s^*(x_s, y_s, z_s) U_s(x_s, y_s, z_s) \rangle, \tag{A.1}$$

where $\langle \ldots \rangle$ indicates the ensemble average, * denotes the complex conjugate operator, and U_s is the monochromatic component of the optical fields at the light source plane $z = z_s$. From the Fresnel diffraction formula, the monochromatic component of the optical fields at any point (X, Y) on the observation plane $z = z_0$ is expressed as

$$U(X, Y, z_0) = \frac{\exp(ikz)}{i\lambda z} \int U_s(x_s, y_s, z_s) \exp\left\{ i \frac{k}{2z} \left[(X - x_s)^2 + (Y - y_s)^2 \right] \right\} dx_s dy_s dz_s, \tag{A.2}$$

where $z = z_0 - z_s$ is the optical depth of the object as measured from the observation plane. In the method given here, the superposed points of the wavefronts are sheared along either the x or y axis. By setting $X = 0$ and $Y = 0$, we may rewrite Eq. (A.2) in the forms

$$U(X, 0, z_0) = \frac{\exp(ikz)}{i\lambda z} \int U_s(x_s, y_s, z_s) \exp\left\{ i \frac{k}{2z} \left[(X - x_s)^2 + y_s^2 \right] \right\} dx_s dy_s dz_s \tag{A.3}$$

$$U(0, Y, z_0) = \frac{\exp(ikz)}{i\lambda z} \int U_s(x_s', y_s', z_s) \exp\left\{ i \frac{k}{2z} \left[x_s'^2 + (Y - y_s')^2 \right] \right\} dx_s' dy_s' dz_s. \tag{A.4}$$

The measured cross-spectral density $W(X, 0, z_0; 0, Y, z_0)$ may be defined as the cross-correlation between the monochromatic components of the optical fields $U(0, Y, z_0)$ and $U(X, 0, z_0)$. It is expressed as

$$
\begin{aligned}
&W(X,0,z_0;0,Y,z_0)\\
&\quad=\langle U^*(X,0,z_0)U(0,Y,z_0)\rangle\\
&\quad=\frac{1}{\lambda^2 z^2}\int\langle U_s^*(x_s',y_s',z_s)U_s(x_s,y_s,z_s)\rangle\\
&\qquad\qquad\times\exp\left\{i\frac{k}{2z}\left[x_s'^2+(Y-y_s')^2-(X-x_s)^2-y_s^2\right]\right\}dx_s dy_s dz_s dx_s' dy_s'. \qquad \text{(A.5)}
\end{aligned}
$$

Because the object is spatially incoherent, the optical fields from different positions on the object are mutually uncorrelated. Thus,

$$
\langle U_s^*(x_s',y_s',z_s)U_s(x_s,y_s,z_s)\rangle = S(x_s,y_s,z_s)\delta^2(x_s-x_s',y_s-y_s'). \qquad \text{(A.6)}
$$

On substituting Eq. (A.6) into Eq. (A.5), we obtain the following expression for the cross-spectral density in terms of the spectral density of the objects:

$$
\begin{aligned}
&W(X,0,z_0;0,Y,z_0)\\
&\quad=\frac{1}{\lambda^2 z^2}\int S(x_s,y_s,z_s)\exp\left[-i\frac{k}{2z}(-x_s^2+y_s^2)\right]\\
&\qquad\qquad\times\exp\left\{i\frac{k}{2z}\left[-(X-x_s)^2+(Y-y_s)^2\right]\right\}dx_s dy_s dz_s\\
&\quad=S'(x_s,y_s,z_s)\otimes\exp\left[i\frac{k}{2z}(-X^2+Y^2)\right]. \qquad \text{(A.7)}
\end{aligned}
$$

Here,

$$
S'(x_s,y_s,z_s)=\frac{1}{\lambda^2 z^2}S(x_s,y_s,z_s)\exp\left[-i\frac{k}{2z}(-x_s^2+y_s^2)\right] \qquad \text{(A.8)}
$$

is the product of the spectral density $S(x_s,y_s,z_s)$ and the phase factor (which depends on the source point). The operator $\otimes$ indicates two-dimensional convolution. The angular cross-spectral density in the Fourier space $\tilde{W}(k_x,0,z_0;0,k_y,z_0)$ is defined as

$$
\begin{aligned}
&\tilde{W}(k_x,0,z_0;0,k_y,z_0)\\
&\quad=\frac{1}{2\pi}\int W(X,0,z_0;0,Y,z_0)\exp\left[-i(-k_x X+k_y Y)\right]dXdY. \qquad \text{(A.9)}
\end{aligned}
$$

Now, the Fourier transform of the second term of the last expression in Eq. (A.7) is expressed as

$$\mathscr{F}\left\{\frac{1}{\lambda^2 z^2}\exp\left[i\frac{k}{2z}(-X^2+Y^2)\right]\right\}$$
$$=\frac{1}{2\pi\lambda^2 z^2}\int\exp\left[i\frac{k}{2z}(-X^2+Y^2)\right]\exp\left[-i(-k_x X+k_y Y)\right]dXdY$$
$$=\frac{\lambda z}{2\pi}\exp\left[-i\frac{z}{2k}(-k_x{}^2+k_y{}^2)\right]. \tag{A.10}$$

This last expression is the OTF defined in 2D Fourier space. Accordingly, on substituting Eq. (A.7) into Eq. (A.9) and applying the convolution theorem, the angular cross-spectral density $\tilde{W}(k_x,0,z_0;0,k_y,z_0)$ is expressed in the following form:

$$\tilde{W}(k_x,0,z_0;0,k_y,z_0)=\frac{\lambda z}{2\pi}\mathscr{F}[S'(x_s,y_s,z_s)]\exp\left[-i\frac{z}{2k}(-k_x{}^2+k_y{}^2)\right]. \tag{A.11}$$

To calculate the inverse propagation, we multiply both sides of Eq. (A.11) by the complex conjugate of the OTF. This is expressed as

$$\tilde{W}(k_x,0,z_0;0,k_y,z_0)\frac{2\pi}{\lambda z}\exp\left[i\frac{z}{2k}(-k_x{}^2+k_y{}^2)\right]=\mathscr{F}[S'(x_s,y_s,z_s)]. \tag{A.12}$$

Now, the inverse Fourier transform of the OTF defined in 2D Fourier space is expressed as

$$\mathscr{F}^{-1}\left\{\frac{2\pi}{\lambda z}\exp\left[i\frac{z}{2k}(-k_x{}^2+k_y{}^2)\right]\right\}$$
$$=\frac{1}{\lambda z}\int\exp\left[i\frac{z}{2k}(-k_x{}^2+k_y{}^2)\right]\exp\left[i(-k_x X+k_y Y)\right]dk_x dk_y$$
$$=\left(\frac{2\pi}{\lambda z}\right)^2\exp\left[-i\frac{k}{2z}(-X^2+Y^2)\right], \tag{A.13}$$

Finally, by taking the inverse Fourier transform of both sides of Eq. (A.12), the final relationship between the spectral density $S'(x_s,y_s,z_s)$ and the cross-spectral density $W(X,0,z_0;0,Y,z_0)$ at the observation plane is obtained as

$$W(X,0,z_0;0,Y,z_0)\otimes\left(\frac{2\pi}{\lambda z}\right)^2\exp\left[-i\frac{k}{2z}(-X^2+Y^2)\right]=\int S'(x_s,y_s,z_s)dx_s dy_s dz_s. \tag{A.14}$$

From these, the absolute value of the left-hand-side of Eq. (A.14) is proportional to the spectral density for a particular light source at $z=$ constant. Therefore, it is possible to

retrieve the spectral component of a 3D image of the light source by this method, which is similar to the conventional angular spectrum technique.

Relevant original papers and proceedings of international conferences

1. Published paper

1) K. Srinuanjan, M. Obara, and K. Yoshimori, "Multispectral hyperbolic incoherent holography," Opt. Rev. **25**, 65-77 (2018).

2. Proceedings of international conferences

1) K. Srinuanjan, S. Ogasawara, M. Obara, and K. Yoshimori, "3D-Spatial and spectral imaging by hyperbolic holography," Proceeding of International symposium on optical memory 2016 (ISOM16), Kyoto, Japan, 16-20 October, 32, (2016).